Nuclear Inst. and Methods in Physics Research, A

Experimental benchmark study of multiphysics simulations of an L- band high average power RF gun

--Manuscript Draft--

Manuscript Number:	NIMA-D-21-00191R1
Article Type:	Full length article
Section/Category:	Accelerators, Beam Handling and Targets
Keywords:	RF gun; average RF heating; multiphysics simulation; experimental benchmark
Corresponding Author:	Guan Shu, Ph.D Deutsches Elektronen-Synchrotron Standort Zeuthen Zeuthen, Zeuthen GERMANY
First Author:	Guan Shu, Ph.D
Order of Authors:	Guan Shu, Ph.D
	Houjun Qian
	Valentin Paramonov
	Namra Aftab
	Prach Boonpornprasert
	Natthawut Chaisueb
	Georgi Georgiev
	James Good
	Matthias Gross
	Christian Koschitzki
	Mikhail Krasilnikov
	Anusorn Lueangaramwong
	Osip Lishilin
	Xiangkun Li
	Sandeep Mohanty
	Raffael Niemczyk
	Anne Oppelt
	Sebastian Philipp
	Frank Stephan
	Hamed Shaker
	Grygorii Vashchenko
	Tobias Weilbach
Abstract:	Multiphysics simulations are widely used in designing high average power RF cavities, which require iterations of RF simulation, thermal simulation and mechanical simulation in a closed loop. The reliability and accuracy of the multiphysics simulations are crucial, otherwise extra design margins are needed for simulation uncertainties. We present an experimental benchmark for the multiphysics simulations of a 40 kW L-band RF gun at the Photo Injector Test facility at DESY in Zeuthen (PITZ). The gun temperature distribution and frequency shift due to average RF heating power are measured and compared with multiphysics simulations.
Suggested Reviewers:	

Opposed Reviewers:	

Experimental benchmark study of multiphysics simulations of an L-band high average power RF gun

G. Shu [a,b,*], H. Qian [a], V. Paramonov [c], N. Aftab [a], P. Boonpornprasert [a], N. Chaisueb [a], G. Georgiev [a], J. Good [a], M. Gross [a], C. Koschitzki [a], M. Krasilnikov [a], A. Lueangaramwong [a], O. Lishilin [a], X. Li [a], S. Mohanty [a], R. Niemczyk [a], A. Oppelt [a], S. Philipp [a], F. Stephan [a], H. Shaker [a], G. Vashchenko [a], T. Weilbach [a]

[a] *Deutsches Elektronen Synchrotron DESY, Platanenallee 6, 15738 Zeuthen, Germany*

[b] *Institute of High Energy Physics, Chinese Academy of Sciences, Beijing 100049, China*

[c] *Institute for Nuclear Research of Russian Academy of Sciences, 60-th October Anniversary prospect 7a, 117312 Moscow, Russia*

Abstract

Multiphysics simulations are widely used in designing high average power RF cavities, which require iterations of RF simulation, thermal simulation and mechanical simulation in a closed loop. The reliability and accuracy of the multiphysics simulations are crucial, otherwise extra design margins are needed for simulation uncertainties. We present an experimental benchmark for the multiphysics simulations of a 40 kW L-band RF gun at the Photo Injector Test facility at DESY in Zeuthen (PITZ). The gun temperature distribution and frequency shift due to average RF heating power are measured and compared with multiphysics simulations.

Keywords: RF gun, average RF heating, multiphysics simulation, experimental benchmark.

1. Introduction

RF photoinjectors are widely used to generate high brightness electron beams for linac based free-electron laser (FEL) light sources [1-7]. The European X-ray Free-Electron Laser (European XFEL) and the Free-electron LAser in Hamburg (FLASH) are pioneers of x-ray laser generation by superconducting linac operating in the long RF pulse mode. To match the long RF pulse length (~1 ms) of the superconducting linac and beam quality requirements of an x-ray free-electron laser, the electron source is a high gradient (~60 MV/m at the cathode) L-band normal conducting RF gun operating in a long pulse mode [8, 9]. Before installing the guns at the European XFEL and FLASH sites, the guns were conditioned and characterized at the Photo Injector Test Facility at DESY in Zeuthen (PITZ) [10]. The main goal of the conditioning is to reach ~60 MV/m cathode gradient at an RF pulse duration of 650 μs and a repetition rate of 10 Hz. This corresponds to an average RF heating power of ~40 kW. In order to further increase the number of x-ray laser pulses generated in one RF pulse, an RF gun with an extended pulse length of 1 ms is requested by FLASH and European XFEL. As a consequence, the average RF heating of the gun is increased by 50% to 60 kW. To meet this challenge, a new generation of RF gun with several improvements was designed, and the first prototype is under fabrication [11]. One of the main improvements is the gun water channel optimization aiming for increased cooling capabilty.

For the high average RF power cavity, water cooling circuit design is essential to reduce overheating, thermal stress and resonant frequency dependence on the RF power. Multiphysics simulations are widely used to verify and optimize the cavity designs, e.g. continuous-wave (CW) radio frequency quadrupole (RFQ) [12], CW buncher [13, 14] and RF gun [11, 15, 16]. With advances of the modern simulation codes and computing power, multiphysics problems of higher complexity can be simulated, which is of vital importance to achieve a reliable simulation result. Results should converge as a sequence of mesh density. Besides, the self-consistent simulations of heat exchange in cooling channels and proper boundary constraints of mechanical structures are critical for reliable simulation of RF heating effects. In the worst case, an unreliable multiphysics simulation may significantly underestimate the RF heating effect, i.e. the cavity temperature rise, the frequency shift and the cavity thermal stress, which will lead to bad vacuum, insufficient frequency tuner range and shorter cavity lifetime. Therefore, multiphysics simulations of RF heating effects are benchmarked with the experiments in this paper.

To benchmark the RF cavity heating effect, measurements of cooling water temperature rise, cavity temperature rise and cavity frequency shift are straightforward, while the measurements of cavity deformation and thermal stress are more difficult. An example of the experimental benchmark study was performed for an RFQ at Japan Atomic Energy Agency (JAEA) [17] with a two-

*guan.shu@desy.de

dimensional approximate analysis. In the simulations, the average temperature of inlet and outlet water was used as the constant cooling temperature, and the heat exchange for vane and wall channels were derived by fitting the measured inlet and outlet water temperature rises. Finally, the 2D simulations reproduced the measured cavity frequency response to water temperature and RF heating. Another benchmark example for DESY gun was presented in Ref. [18, 19]. The heat transfer coefficients based on the empirical equations were used in the 3D simulations. This is an engineering approach which assumes a uniform cooling channel and homogenous water speed in the channel cross section. The simulated iris temperature rise was ~20% underestimated compared to the measured value. Later on, the heat transfer coefficient distribution simulated by the computational fluid dynamics (CFD) software was adopted in the RF cavity design [20]. Unlike the uniform distribution derived from the empirical approach, the simulated heat transfer coefficient between water and cavity reflects the nonuniform distributions of water flow speed and cooling channel dimensions. Since the simulated heat transfer coefficient is more close to the cooling channel reality than the engineering approach, it is more precise to describe the heat exchange between cavity and cooling water. For example, it was adopted in the thermal simulations of the latest 60 kW DESY gun [11] and the 400 Hz S-band RF gun at STFC Daresbury Laboratory [20].

In this paper, an experimental benchmark of multiphysics simulations for the DESY 40 kW L-band normal conducting RF gun is presented. The paper is organized as follows. In Section 2, a brief description of the gun system is presented. Section 3 illustrates the detailed numerical simulations of the gun. In Section 4, the high power experimental procedures, results and error analysis are reported. The comparison between simulations and measurement results are shown. Section 5 gives a brief discussion on the usage of multiphysics simulations in designing an RF cavity.

2. Brief introduction to the DESY L-band normal conducting RF gun

The DESY L-band RF gun of 4th generation (Gun 4) consists of a 1.6 cell copper cavity surrounded by a stainless steel jacket. The schematic view of the gun is shown in Fig. 1. The cathode plug is inserted into the cavity backplane through a load lock system without breaking the vacuum. The RF power is fed into the cavity from a 10 MW multi-beam klystron via a hollow waveguide (WR-650) to a 'doorknob' type coaxial coupler. The gun is normally conditioned up to a peak power of ~6 MW at a pulse duration of 650 μs and a repetition rate of 10 Hz, corresponding to a ~6 MeV beam with a peak acceleration field of ~60 MV/m at the cathode. The maximum average RF power dissipated in the cavity is up to ~40 kW. The gun has implemented 14 cooling channels (see Fig. 1) for heat removal and resonance control. The water channel distributions are arranged according to the surface heat flux distribution aiming for a high heat transport efficiency and a uniform temperature distribution. The latter one is meant to reduce the temperature gradient in the cavity body hence a smaller structure stress. Each channel is equipped with a water flow meter allowing monitoring and control of the water flow. Numerous temperature sensors are mounted to record the gun body and cooling water temperatures. One of the temperature sensors inside the gun central iris disk serves for the water temperature feedback system for stable operation. The cavity frequency tuning at various average power levels is realized by adjusting the inlet water temperature while the water flow is kept constant. The water flow velocity in the cooling channels is ~2 m/sec, and the total water consumption is ~12 m^3/h in routine operation.

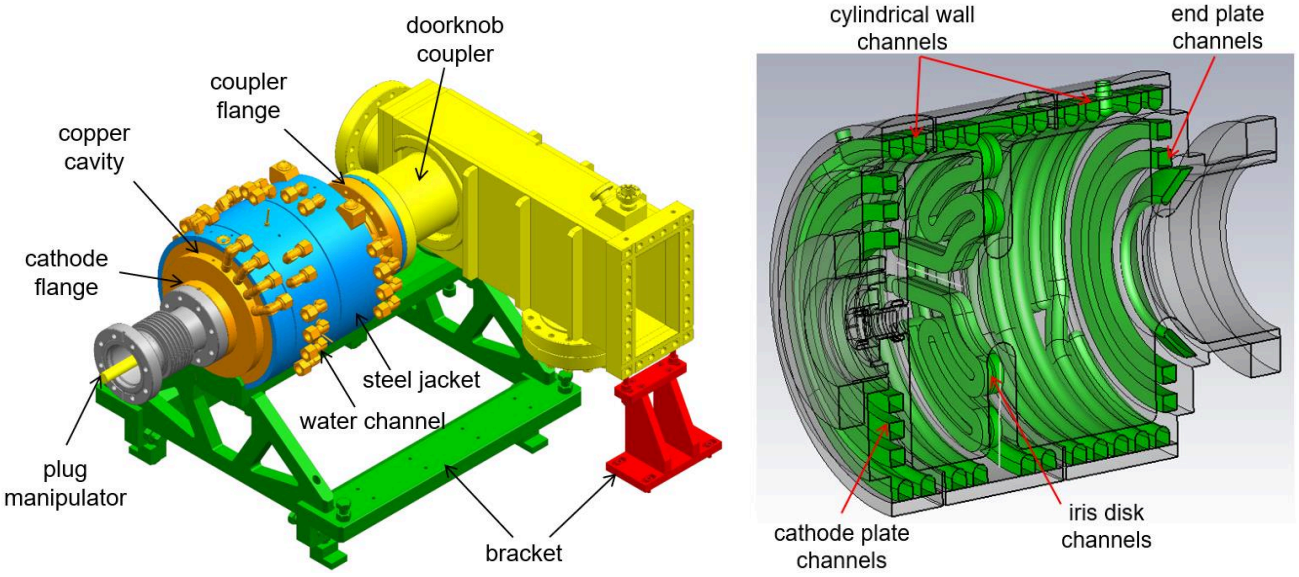

Fig. 1. Schematic view of the DESY Gun 4 assembly (left) and cooling channel distributions (right).

3. Multiphysics analysis of the RF gun

Since the RF gun operates in a long pulse mode, both the average RF heating and pulsed heating effect are of paramount importance for the long term operation reliability and stability. The details about the pulsed heating analysis can be found in Ref. [21, 22]. The measurements and the benchmark simulations in this paper focus on the average RF heating effect. The material properties used in the simulations are listed in Table 1. The mechanical analysis adopts the linear elastic modulus because the maximum stress under a power level of 40 kW in the following simulations is less than the yield strength limit of the material.

Table 1. Material parameters of the gun body in the simulations.

Parameters	OFHC copper	Stainless steel
Thermal conductivity [W/m/K]	391	16.3
Thermal expansion coefficient [1/K]	1.67×10^{-5}	1.59×10^{-5}
Young's modulus [GPa]	123	193
Poisson ratio	0.345	0.28
Electrical conductivity [S/m]	5.8×10^{7}	N/A

3.1 Multiphysics simulation methodology

The multiphysics simulations comprise the integrated electromagnetic, thermal and mechanical simulations, as shown in Fig. 2. The RF simulations were performed by using CST MICROWAVE STUDIO (CST MWS) version 2019 [23], and the thermal and mechanical simulations were conducted by CST MULTIPHYSICS STUDIO (CST MPS) [23]. The coupled simulations were also carried out with ANSYS workbench version 20.1 [24] for comparison.

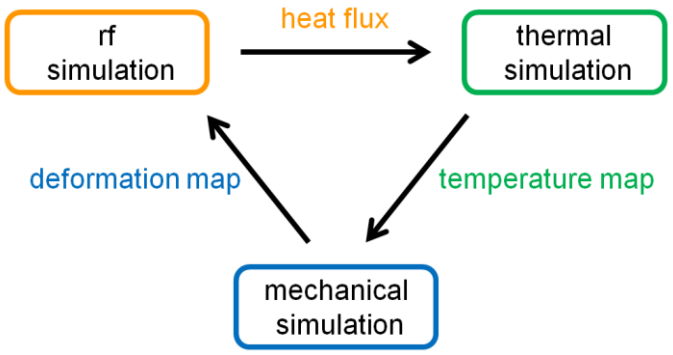

Fig. 2. Schematic workflow of the multiphysics simulations.

The RF simulation was first initiated to obtain the field distribution of the resonant π mode, thereby calculating an initial resonance frequency. The heat flux generated by RF field is determined by the surface magnetic field strength, which can be described as [25]:

$$P_c = \frac{1}{2}\sqrt{\frac{\pi f_0 \mu_0}{\sigma}}|H_t|^2 \quad (1)$$

where f_0 denotes cavity frequency, μ_0 is the vacuum permeability, σ is the electric conductivity of copper and H_t is the inner surface magnetic field amplitude. The internal surface power loss density distribution simulated by CST MWS is shown in Fig. 3. When the total power loss is scaled to 40 kW, the maximum thermal loss density is 29.7 W/cm^2. The RF simulations with ANSYS gave a similar power loss distribution.

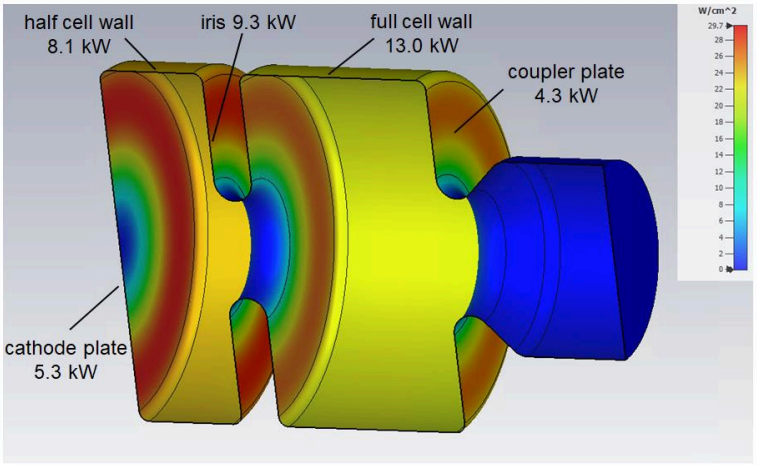

Fig. 3. Surface power loss density distribution with a total power loss of 40 kW (simulated by CST MWS).

Then, the heat flux map is transferred to the thermal module to evaluate the steady-state temperature distribution. The heat exchange between water and cavity plays a significant role in the temperature simulation and the following cavity deformation and frequency shift. Therefore, it must be precisely defined in the thermal analysis. Two options are usually used for the heat transfer coefficient calculation: an empirical equation and fluid dynamics simulations.

The empirical heat transfer coefficient α can be expressed as [26]:

$$\alpha = \lambda \cdot Nu/d \tag{2}$$

where λ is the thermal conductivity of the water, Nu is the dimensionless Nusselt number and d is the hydraulic diameter which is calculated from the area and wetted perimeter of the flow cross-section.

A criterion for turbulent water flow in a water tube is given by the Reynolds number [26]:

$$Re = \frac{V_m \cdot d}{\nu} \tag{3}$$

where V_m is the fluent velocity and ν is the kinematic viscosity. The water in the Gun 4 is in the turbulent regime (Re $\geq$ 10000) and Nu can be calculated by [26]:

$$Nu = 0.023 \cdot Re^{0.8} \cdot Pr^{0.4} \tag{4}$$

$$Pr = \frac{\eta C_p}{\lambda} \tag{5}$$

where Pr is the Prandtl number, η is the dynamic viscosity and C_p denotes the specific heat capacity of the fluid. The fluent velocity in one channel can be calculated from the flow rate and the cross-section area. Both CST MPS and ANSYS can do thermal simulations by using the empirical heat transfer coefficient. The water temperature at the water-pipe interface is assumed to be constant, not considering the water temperature rise along the cooling channel. The average temperature of inlet and outlet water is used in the simulations as an approximation. Besides, the heat transfer coefficients in one channel are assumed to be constant, not considering water velocity changes near the corners.

For a heavy heat loaded cavity with complex cooling channels like the Gun 4, the fluid dynamics simulation via ANSYS CFX code is more close to reality and therefore preferred. The variations of water temperature and flow velocity in the cooling channels can be reflected in the simulations, providing more precise heat exchange compared to simplified calculations based on empirical formulas. The simulation results are shown in Fig. 4 and 5. The average water speed in the channels is ~2 m/s. Due to the channel inhomogeneity, the size of the inlet and outlet cylindrical pipe is smaller than the rest part leading to a relatively higher local water speed as well as a higher local heat transfer coefficient. The water speed near the 180° bend outer corner vicinity is slow (less than 1 m/s). As a result, the surface heat transfer factor in this vicinity is only ~30% of the average value of the whole channel. The empirical heat transfer factor of each channel is 10~20% higher than the average value simulated by CFX (see Fig. 5). The detailed cavity temperature distributions with these two calculation methods are presented in the following sections.

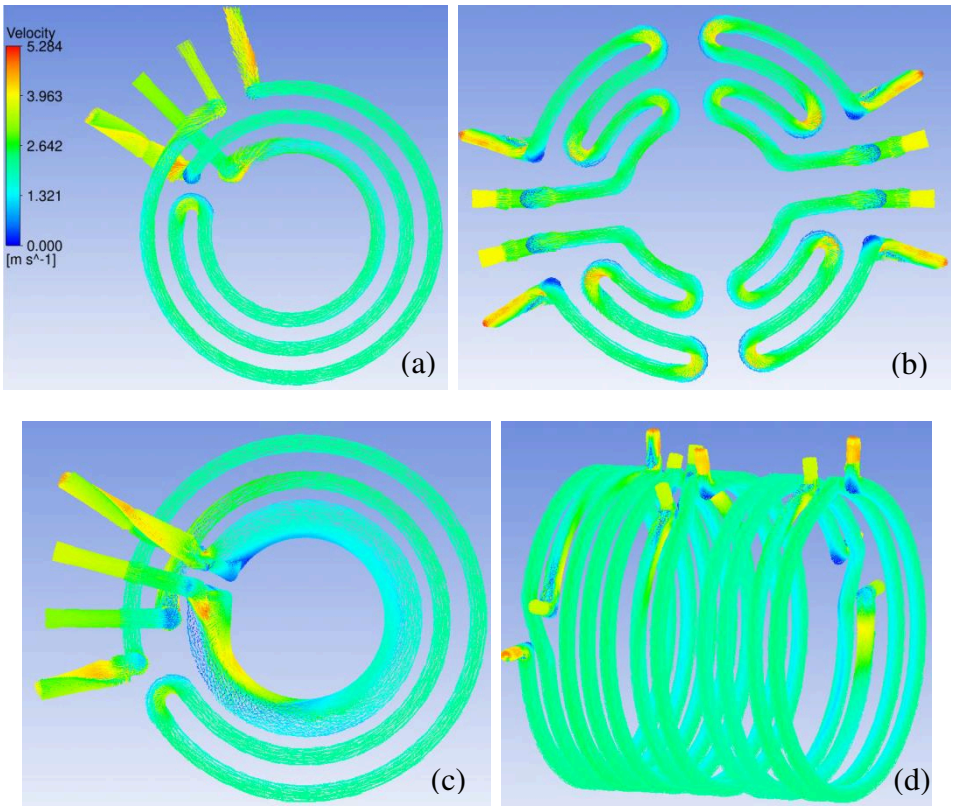

Fig. 4. Simulated water speed distributions by using the flow rate in operation (12 m^3/h total water flow): flow velocity in the channels of (a) cathode plate, (b) iris disk, (c) end plate, (d) cylindrical wall.

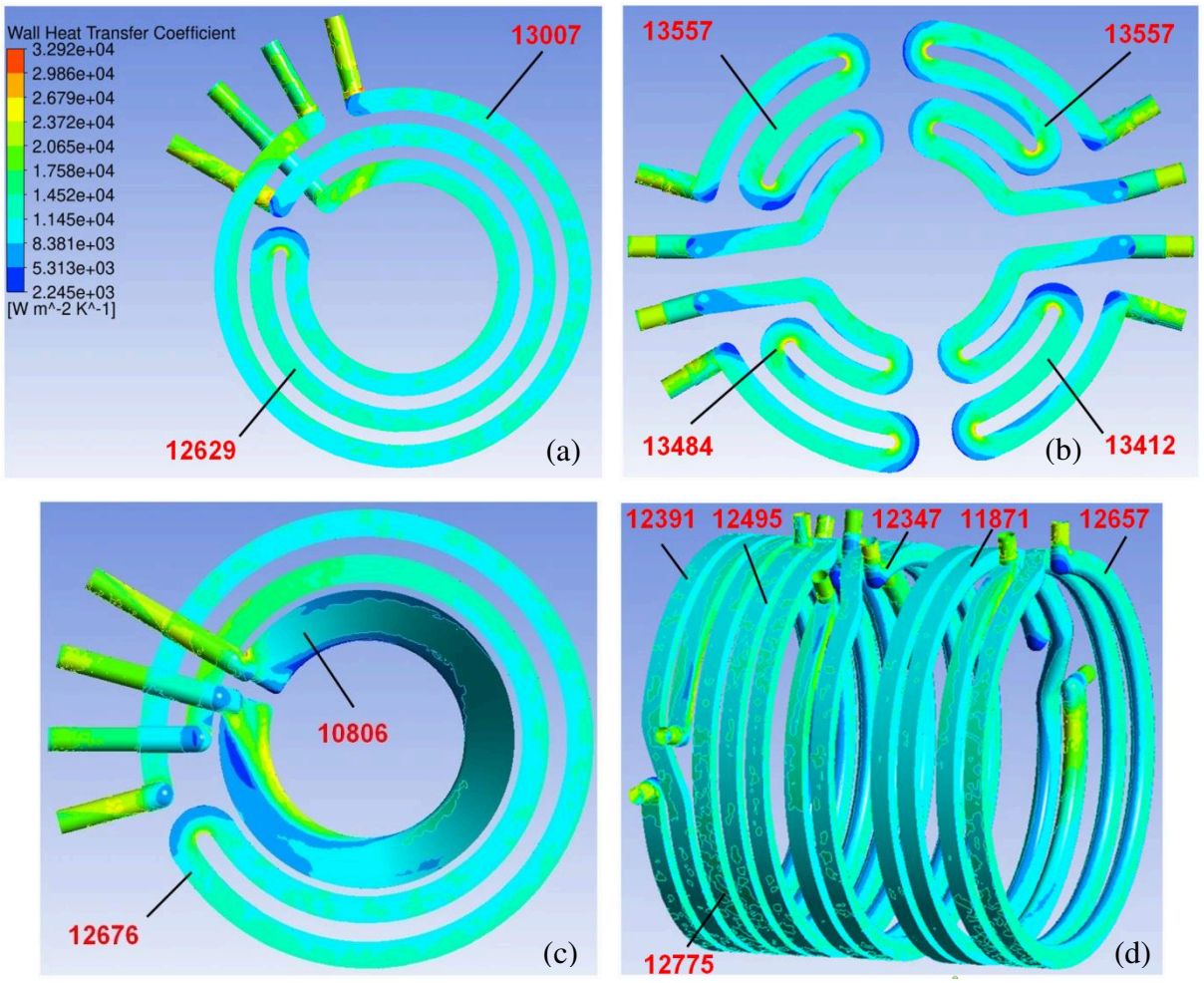

Fig. 5. Simulated heat transfer coefficient distributions in the channels of (a) cathode plate, (b) iris disk, (c) end plate, (d) cylindrical wall. The cooling conditions in operation (~70°C water temperature and 12 m^3/h total water flow) were used in simulations. The numbers in red represent the empirical calculation for comparison.

For the mechanical simulation, the cavity deformation is evaluated based on the thermal expansion coefficient of the material and the temperature rise w.r.t the reference value. The induced stress depends on the temperature gradient, material properties and cavity geometry shape. Besides, the boundary constraints of the structure will also affect the deformation distributions and therefore structure stress and cavity frequency shift, so the boundary constraints should be defined as realistically as possible.

In the last step, the resonant frequency is calculated again with the deformed shape in the RF simulations to estimate the resonant frequency shift.

During the coupled simulations, the mesh quality in each module and the mesh matching between modules are also critical for reliable results. It is necessary to find a proper mesh definition by a mesh convergence study. In the benchmark simulations, the total mesh cell number in each module is in several million scales.

3.2 Water temperature effect on the gun frequency

Since no mechanical frequency tuners exist in the RF gun, the water temperature is used for tuning the cavity frequency at various RF heating loads. In the free expansion approximation, the relationship between frequency shift Δf and temperature change ΔT is:

$$\Delta f = \alpha f_0 \Delta T \tag{6}$$

where α is the material thermal expansion coefficient shown in Table 1, f_0 is the operating frequency1300 MHz. The gun consists of a copper cavity surrounded by a stainless steel jacket. Since the thermal expansion coefficients of copper and steel are not identical, the theoretical temperature detuning sensitivity is in the range of 20.7 - 21.7 kHz/°C. Once the gun is installed in the beamline, the expansion with external constraints is difficult to be calculated analytically due to the complex external constraints. Therefore measurements were performed at PITZ to study the gun frequency dependence on cooling water temperature. A feed-forward phase modulation was implemented in the low level RF (LLRF) system allowing us to adjust the klystron output frequency within the klystron bandwidth. The frequency offset was scanned to match the gun resonant frequency, and thus minimizing the reflected power. Therefore, the gun frequency shift at various water temperatures can be tracked. In the measurements, the gun was fed swith a 200 μs and 10 Hz RF pulse with a peak power of 4.8 MW. The corresponding average RF power loss was ~10 kW. The inlet water temperature was scanned in a range of 4°C. The dependence of gun frequency shift on the inlet water temperature is shown in Fig. 6. The water temperature detuning sensitivity was measured to be 21.8 kHz/°C.

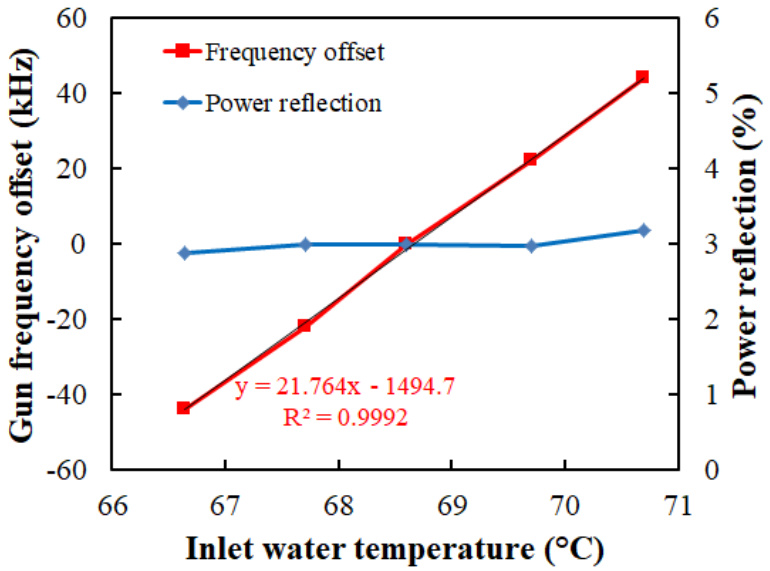

Fig. 6. Forward RF frequency offset w.r.t. 1300 MHz versus different inlet water temperature. For each temperature, the gun forward peak power was kept at 4.8 MW and the power reflection was kept at 3%.

In the benchmark simulations, we considered two possible mechanical boundary conditions. One is the longitudinally fixed boundary only on the coupler flange (see Fig. 1), considering a hard constraint from the coupler waveguide and a negligible soft constraint from the cathode flange with a bellow. The other one is the longitudinally fixed constraints on both the coupler side and the cathode flange. The first boundary setting indicates similar features as free boundaries. The gravity was not included in the simulations due to its relatively small cavity weight.

Table 2. Water temperature effect on gun frequency with different boundaries and software.

	Longitudinally fixed at coupler flange	Longitudinally fixed at coupler and cathode flange
CST [kHz/°C]	21.2	28.1
ANSYS [kHz/°C]	21.2	28.3

Table 2 summarizes the simulation results of the water temperature effect on gun frequency. A high-quality mesh was generated in both codes based on the mesh convergence study. As a consequence, the CST result agrees well with ANSYS. The longitudinally fixed constraint at the coupler flange proves to be closer to the measurements. Therefore, the same boundary was applied to the model in the following mechanical simulations.

3.3 Average RF heating effect

An inlet water temperature of 70°C was set as the reference temperature in the thermal and mechanical simulations, and the average power dissipated on the inner surface was set to 40 kW. The cavity heat removal is accomplished through air and water cooling. The free convection between gun and air is typical ~5 W/(m^2·K) which implies little influence on the thermal conduction. The water flow measured in each channel was used to calculate the heat transfer coefficient. In the thermal simulation with empirical heat transfer coefficient, the water temperature rise between inlet and outlet water was included. The average water temperature rise was calculated to be 2.9°C based on the 40 kW power dissipation and the 12 m^3/h water flow. Then, the average value of inlet water and outlet water temperature was applied to the cooling channels. The distributions of temperature, deformation and stress by using empirical and ANSYS CFX simulated heat transfer coefficients are shown in Fig. 7.

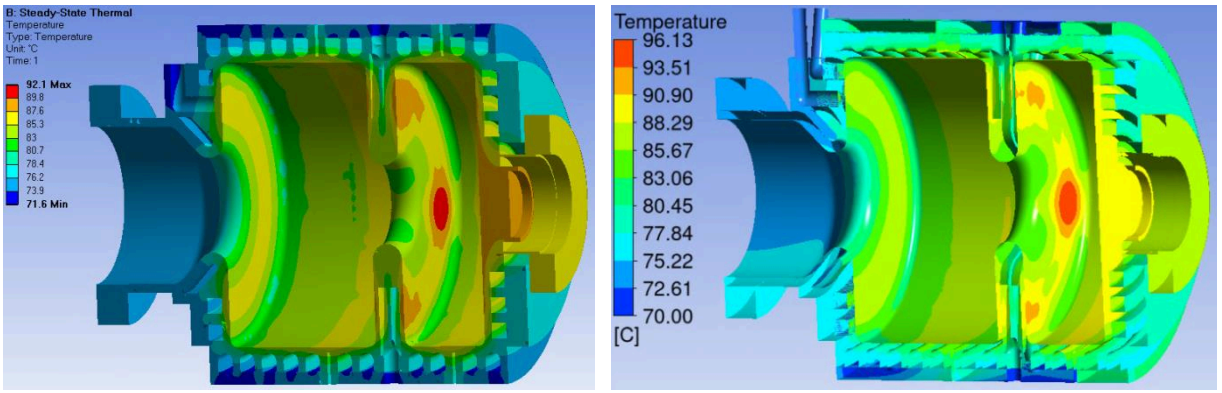

(a) gun temperature distribution

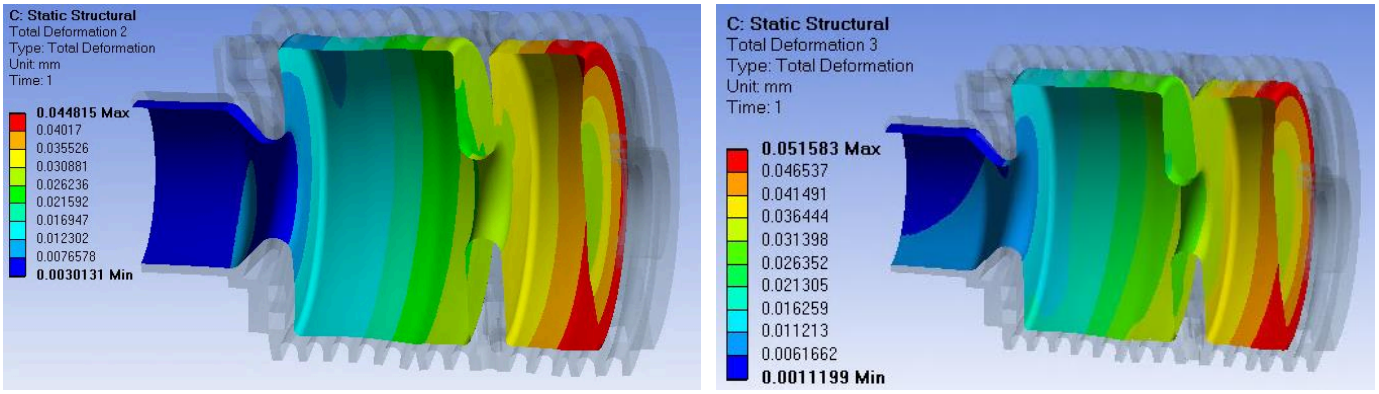

(b) inner surface deformation distribution

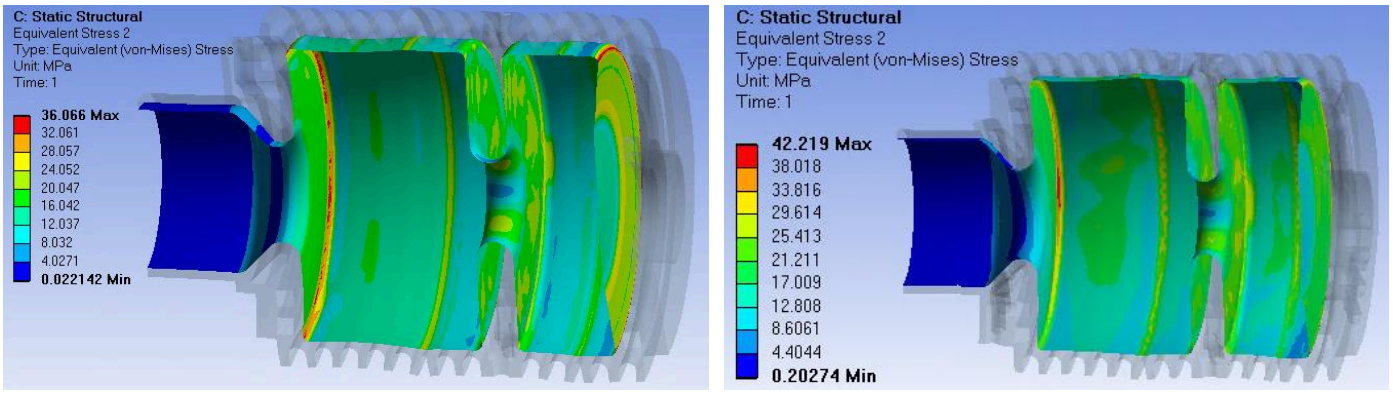

(c) von-Mises stress distribution at the inner surface

Fig. 7. ANSYS simulation results with the empirical heat transfer coefficient (left) and CFX simulated heat transfer coefficient (right) under 40 kW RF heating: (a) temperature distribution, (b) inner surface deformation, (c) inner surface von-Mises stress distribution.

Table 3 lists the main parameters of the RF heating effect on the gun cavity by using different codes and different heat exchange definitions. Simulations using the same empirical heat transfer coefficient show consistent results between CST and ANSYS. The average copper temperature rise obtained with CFX simulated heat transfer coefficient is 20% higher than that obtained with empirical one. As a consequence, the thermal expansion induced cavity deformation and frequency shift are also 20% higher by using CFX simulated heat transfer coefficient than empirical approach. The deviation is attributed to the 10~20% overestimated empirical heat transfer coefficient w.r.t the CFX simulated value, as mentioned in Section 3.1

Table 3. Comparison of RF heating effect on gun frequency by using different codes and different heat exchange definitions.

Parameters	CST with empirical heat transfer coefficient	ANSYS with empirical heat transfer coefficient	ANSYS with CFX simulated heat transfer coefficient
Average power loss [kW]	40	40	40
Average copper temperature rise w.r.t inlet water temperature [°C]	9.7	9.8	11.7
Average inner surface deformation [μm]	24.1	23.2	28.6
Maximum von Mises stress [MPa]	33.1	36.1	42.2
Frequency shift [kHz]	-226.0	-227.3	-274.5
Detuning sensitivity due to RF heating [kHz/kW]	-5.7	-5.7	-6.9

4. High power benchmark measurements

In order to benchmark the simulation results in Section 3.3, high power RF measurements were conducted with the RF gun at PITZ to measure its frequency shift sensitivity to RF heating. In this experiment, the peak power of the RF gun was fixed, and the RF pulse length was varied to change the average RF heating of the gun. The inlet water temperature was used as a frequency tuner to keep the cavity resonant at 1300 MHz at various average power levels with an RF reflection of ~3%, compensating the frequency shift induced by RF heating. Then the cavity frequency change due to the RF heating can be measured with the inlet water temperature change, with a measured sensitivity of 21.8 kHz/°C.

In the measurements, the cathode gradient (57 MV/m) was kept unchanged and the pulse length was scanned from 200 μs to 400 μs with a step of 50 μs. Two methods were used to calculate average power loss at different pulse length. The first one is a straightforward approach by using the inlet and outlet water temperature rise in combination with total water flow. The measurements are shown in Fig. 8. The inlet-outlet temperature rise was increased by only 0.76°C for the 200 μs pulse length case, but a peak to peak temperature fluctuation of ~0.2°C from sensors reading was observed, introducing a significant uncertainty of the RF heating calculation. A detailed error analysis is presented at the end of this section.

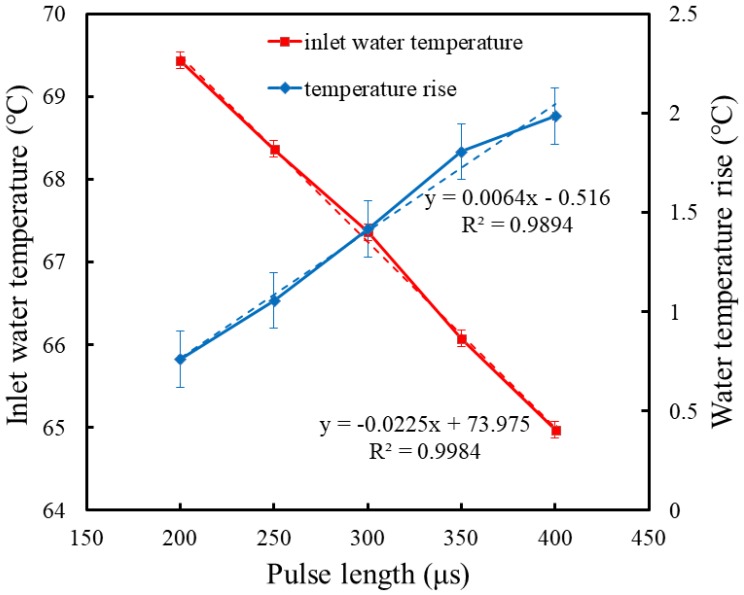

Fig. 8. Inlet water temperature and water temperature rise between inlet and outlet versus RF pulse length.

The second approach is based on the beam energy measurement and the cavity RF properties . The cavity voltage was obtained by the beam energy measurements through a spectrometer dipole magnet in the beamline [8]. The cavity shunt impedance was calculated based on the simulated cavity R/Q and measured unloaded quality factor Q_0. The cavity Q_0 was measured before installing in the beamline. We can also measure Q_0 via the LLRF system when the gun is in operation. Finally, the average cavity power is calculated based on the beam energy, cavity shunt impedance, Q_0 and cavity duty factor, as shown in Eq. (7):

$$P_c = \frac{V_{beam}^2}{\left(\frac{R}{Q}\right)Q_0} DF \tag{7}$$

where V_{beam} is the cavity voltage measured by the maximum beam energy gain, R/Q is simulated from cavity geometry, DF is the RF duty factor of the cavity. The accuracy of the RF heating calculation depends on the beam energy and Q_0 measurements.

The gun Q_0 was measured to be 20472 by a vector network analyzer (VNA) at a room temperature (~20°C). The operation temperature of the current gun is ~70°C resulting in a lower Q_0 because the copper conductivity reduces with rising temperature. With the cavity filling time calculated from the reflected power decay slope (see Fig. 9) and the cavity coupling factor calculated from the smith chart program in the LLRF system, one can obtain the online measurement of Q_0. The simulations and measurements are listed in Table 4. The difference between the LLRF online measurement and the scaled results from offline VNA measurement is only 5%. A Q_0 of 19195 (average of VNA measurement and LLRF measurement) with an error of +/- 480 is used in the following analysis. The measured Q_0 is ~10% lower than the ideal simulation values at 70 °C, which is reasonable in cavity development.

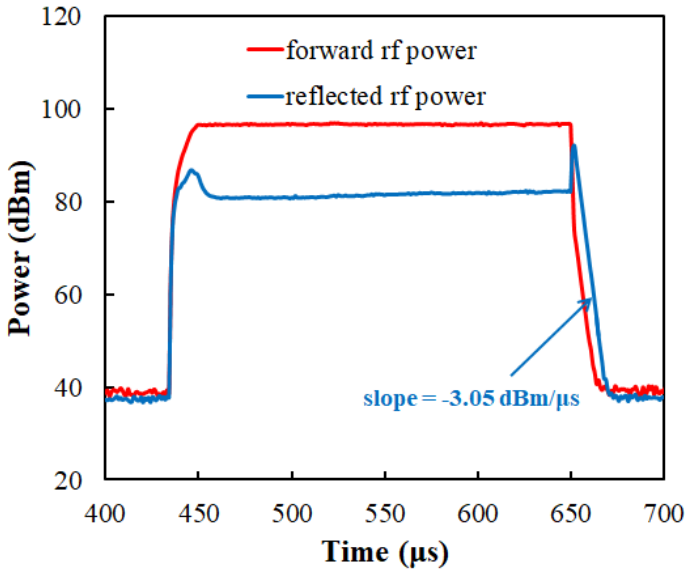

Fig. 9. Forward and reflected RF power waveform extracted from the directional couplers. The decay slope of the reflected power is -3.05 dBm/μs, corresponding to the cavity filling time constant of 2.84 μs.

Table 4. Unloaded quality factor Q_0 simulations and measurements.

	Simulation at 20°C (Cu conductivity = 5.80E7 S/m)	Simulation scaled to 70°C (Cu conductivity = 4.86E7 S/m)	VNA measurement at room temperature ~20°C	VNA measurement scaled to 70°C	LLRF measurement in high power at 70°C
Q_0	23240	21246	20472	18715	19674

Fig. 10(a) shows the average power loss as a function of the RF pulse length by using the previously mentioned two approaches. The error bar of the red dotted curve corresponds to the +/- 0.1°C peak to peak water temperature measurement fluctuation. The error bar of the black line corresponds to the +/- 480 error in Q_0 measurements. The power measurement results by the two approaches are barely within their error bars. Fig. 10(b) shows the cavity frequency shift induced by the RF heating. The cavity frequency sensitivity to RF power is fitted to be -7.11 ± 0.43 kHz/kW based on the power measured by the cavity Q_0 and beam energy, and -5.50 ± 0.78 kHz/kW based on the power measured by the water temperature rise. Due to the large uncertainty caused by the water temperature measurement, the frequency sensitivity of -7.11 ± 0.43 kHz/kW is more reliable. The simulation result of -6.9 kHz/kW based on the CFX simulated heat transfer coefficient in Table 3 is in better agreement with the measurement than simulations with empirical heat transfer coefficient.

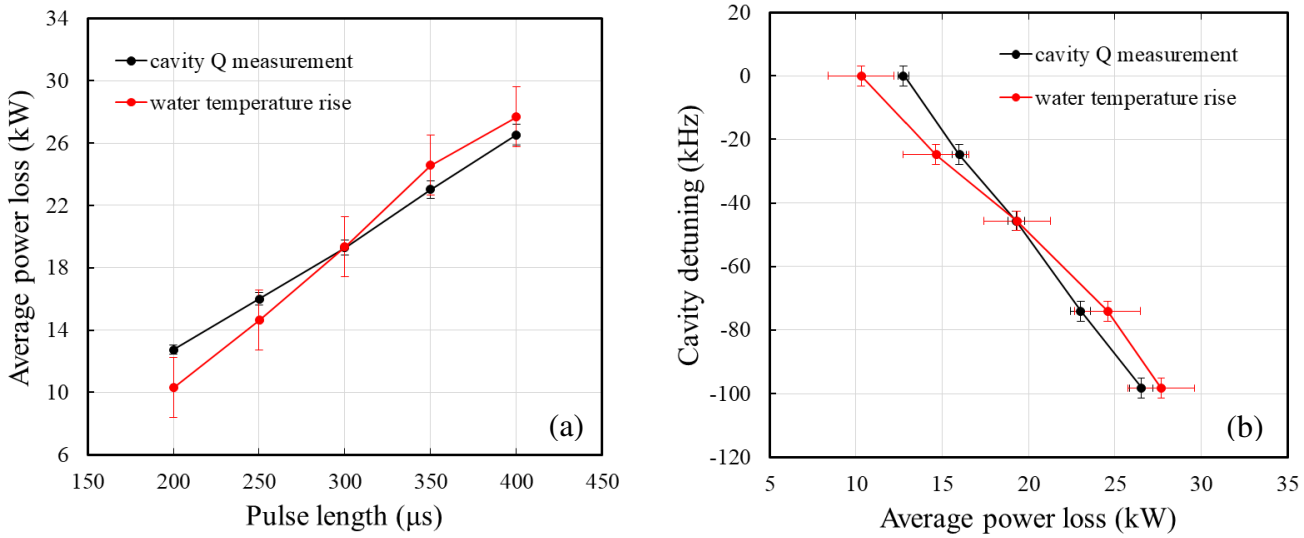

Fig. 10. (a) average power loss vs. pulse length, (b) cavity detuning vs. average power loss.

A few temperature sensors are placed inside the middle iris and one of them is used as a feedback for a water temperature regulation system. The comparison between sensor measurements and ANSYS simulations with empirical and CFX simulated heat transfer coefficients is shown in Fig. 11. The RF pulse length in the measurement was 300 μs and the average power loss was calculated to be 18 kW. Again, the overestimation of heat transfer coefficients based on empirical formulas leads to a lower temperature rise compared to the simulated heat transfer coefficients. The sensor temperature values are shown in Fig. 11 by red numbers. From the sensor calibration test, the bottom sensor in Fig. 11 indicated a worse performance than the other three, therefore it might be damaged by radiation from the gun. One contribution to the discrepancy between the top three sensor measurements and simulations can be the sensor calibration error. In addition, the thermal contacts from the surrounding parts (e.g. load-lock system, doorknob coupler and support bracket) were ignored in the simulation, which leads to an overestimation on simulated temperature. The details of the sensor installation were also ignored in simulation, which might be another reason for the discrepancy. Since the accuracy of the gun frequency measurement is much higher than gun iris temperature measurement, the benchmark of frequency sensitivity is more reliable than temperature.

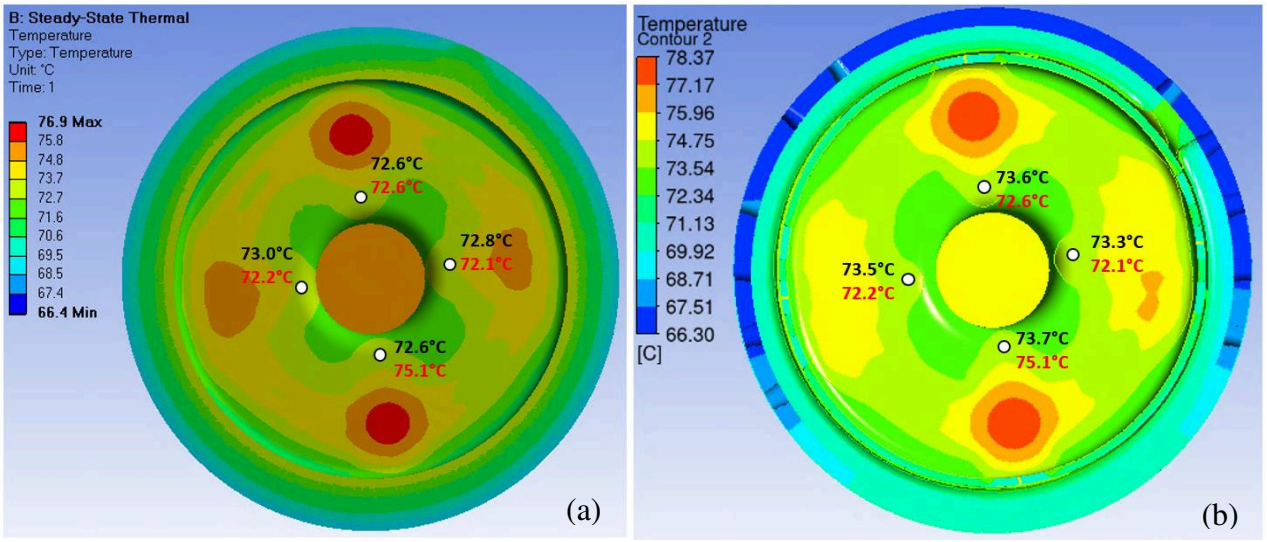

Fig. 11. Iris temperature distribution calculated from ANSYS with (a) empirical heat transfer coefficient and (b) CFX simulated heat transfer coefficient. The simulated temperatures at the sensor position are marked in black. Temperature measurements in experiments are marked in red for comparison.

5. Discussion

The heat transfer coefficient is of paramount importance in multiphysics simulations of RF cavities. If a high power experiment is available, we can evaluate the heat exchange between water and cavity by data fitting with the experiment, which was adopted in Ref. [17]. In the design stage, the precise heat transfer coefficient definition is crucial to obtain reliable predictions. In case of the benchmark simulations of the Gun 4, the heat transfer coefficient calculated from the empirical approximation is overestimated by ~20%. As a consequence, the cavity temperature rise, deformation and frequency shift are underestimated by ~20%. In contrast, the benchmark simulation with the heat transfer coefficient derived from ANSYS CFX simulation is in much better agreement with the experiments. Therefore, the simulated heat transfer coefficient is preferred in the design stage to predict the cavity performance in the high average RF power regime. However, the CFX simulation always takes a long time to reach convergence which is tedious in the cooling channel optimization. The empirical approach is more suitable in the optimization process. Another critical point in the thermal simulation with the empirical approach is the water temperature definition. For the low average power cavity, in which the water temperature rise in the channel can be ignored, the inlet water temperature can be applied on the channel surface in the simulation. For a heavy RF loaded cavity like the Gun 4, the inlet to outlet temperature rise is ~30% of the gun average temperature rise. The mean value of the inlet and outlet temperature should be used, otherwise the average gun temperature will be underestimated.

6. Conclusion

We performed an experimental benchmarking of the integrated multiphysics simulations for the DESY Gun 4, including the electromagnetic, thermal and mechanical simulations. The multiphysics simulations are done with two codes, CST and ANSYS. The heat transfer coefficient calculation in the thermal module proves to be most critical. The multiphysics simulations with empirical values underestimate the RF heating induced temperature rise, deformation, stress and frequency detuning by ~20% for the Gun 4. The simulation results with CFX simulated heat transfer coefficient agree well with measurements. For the cooling analysis of a heavy heat load cavity, the simulated heat transfer coefficient is highly recommended for more accurate results, based on which a more appropriate safety margin can be used in engineering designs.

Acknowledgements

We would like to thank S. Lal, W. Koehler and J.Schultze for valuable discussions. This work was supported by the European XFEL research and development program. The numerical simulation research was supported in part through the European XFEL and DESY funded Maxwell computational resources operated at Deutsches Elektronen-Synchrotron (DESY), Hamburg, Germany.

Reference

[1] W. Decking, et al., A MHz-repetition-rate hard X-ray free-electron laser driven by a superconducting linear accelerator,

Nature Photonics (2020): 1-7.
[2] S. Siegfried and B. Faatz, The free-electron laser FLASH, High Power Laser Science and Engineering 3 (2015).
[3] R. Akre, et al., Commissioning the linac coherent light source injector, Phys. Rev. ST Accel. Beams, 11 (2008), 030703.
[4] T. Schietinger, et al., Commissioning experience and beam physics measurements at the SwissFEL Injector Test Facility, Phys. Rev. Accel. Beams, 19 (2016), 100702.
[5] D. Angal-Kalinin, et al., Design, specifications, and first beam measurements of the compact linear accelerator for research and applications front end, Physical Review Accelerators and Beams, 23 (2020), 044801.
[6] G. Penco, et al., Optimization of a high brightness photoinjector for a seeded FEL facility, Journal of Instrumentation, 8(05), P05015.
[7] F. Sannibale, et al., Advanced photoinjector experiment photogun commissioning results, Physical Review Special Topics-Accelerators and Beams, 15 (2012), 103501.
[8] F. Stephan, et al., Detailed characterization of electron sources yielding first demonstration of European X-ray Free-Electron Laser beam quality, Phys. Rev. ST Accel. Beams, 13 (2010), 020704.
[9] M. Krasilnikov, et al., Experimentally minimized beam emittance from an L-band photoinjector, Phys. Rev. ST Accel. Beams, 15 (2012), 100701.
[10] I. Isaev, et al., Conditioning status of the first XFEL gun at PITZ, 35th Free Electron Laser Conf. (FEL'13), New York, USA, 26-30 August 2013.
[11] V. Paramonov, et al., Design of an L-band normally conducting RF gun cavity for high peak and average RF power, Nuclear Instruments and Methods in Physics Research Section A: Accelerators, Spectrometers, Detectors and Associated Equipment 854 (2017): 113-126.
[12] S. V. Kutsaev, et al., Design and multiphysics analysis of a 176 MHz continuous-wave radio-frequency quadrupole, Physical Review Special Topics-Accelerators and Beams, 17 (2014), 072001.
[13] G. Romanov, et al., CW room temperature re-buncher for the Project X front end, Conf. Proc. C1205201: 3880-3882, 2012. No. FERMILAB-CONF-12-129-TD.
[14] T. Takahashi, et al., Development of a 1.3-GHz buncher cavity for the compact ERL, Proc. 5th International Particle Accelerator Conf.(IPAC 2014), Dresden, Germany, 15-20 June 2014.
[15] R. P. Wells et al., Mechanical design and fabrication of the VHF-gun, the Berkeley normal-conducting continuous-wave high-brightness electron source, Review of Scientific Instruments, 87 (2016), 023302.
[16] G. Shu, et al., Multiphysics Analysis of a CW VHF Gun for European XFEL, 39th Free Electron Laser Conf.(FEL'19), Hamburg, Germany, 26-30 August 2019.
[17] Y. Kondo, et al., High-power test and thermal characteristics of a new radio-frequency quadrupole cavity for the Japan Proton Accelerator Research Complex linac, Physical Review Special Topics-Accelerators and Beams 16 (2013), 040102.
[18] K. Floettmann, et al., RF Gun cavities cooling regime study, DESY report, TESLA-FEL, 2, 2008.
[19] F. Marhauser, Finite element analyses for RF photoinjector gun cavities, DESY report, TESLA-FEL, 2, 2006.
[20] B. L. Militsyn, et al., Design of the high repetition rate photocathode gun for the CLARA project, in Proceedings of LINAC'14, Geneva, Switzerland, 31 August-05 September 2014.
[21] V. Paramonov, A. Skasyrskaya, Pulsed RF heating simulations in normal conducting L-band cavities, DESY, Hamburg, Rep. TESLA-FEL 2007-04, 2007.
[22] D. Pritzkau, RF Pulsed Heating, Ph. D Thesis, SLAC-R-577, 2001.
[23] CST Simulation packages, http://www.cst.com.
[24] ANSYS, http://www.ansys.com.
[25] T.Wangler, RF Linear Accelerators[M]. RF Linear Accelerators, by Thomas Wangler, pp. 397. ISBN 0-471-16814-9. Wiley-VCH, May 1998. 2008.
[26] F. Kreith, The CRC Handbook of Thermal Engineering (CRC Press, Boca Raton, 2000).

Figure 1(left)

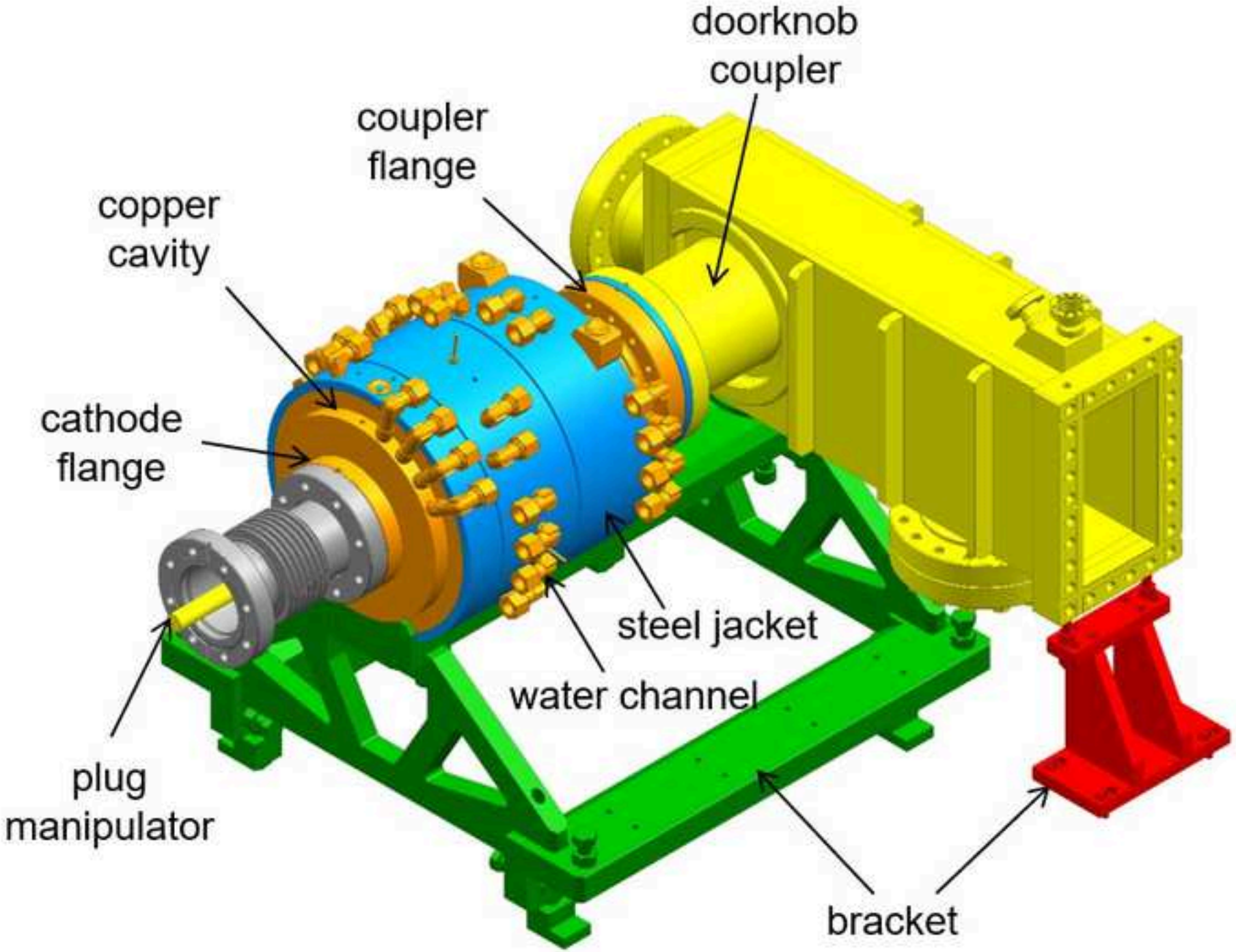

Figure 1(right)

Click here to access/download;Figure;Fig 1(right).jpg

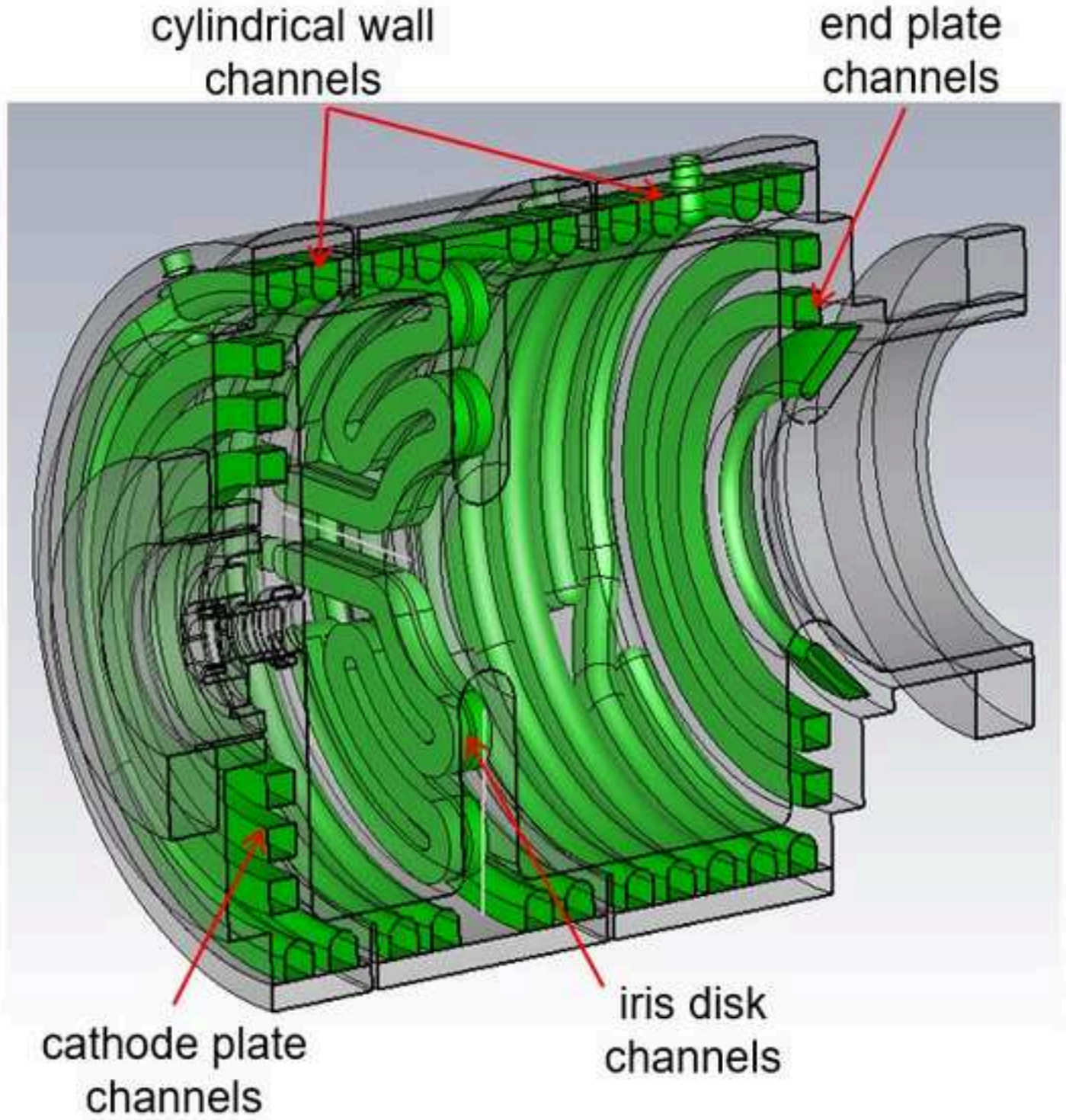

Figure 2

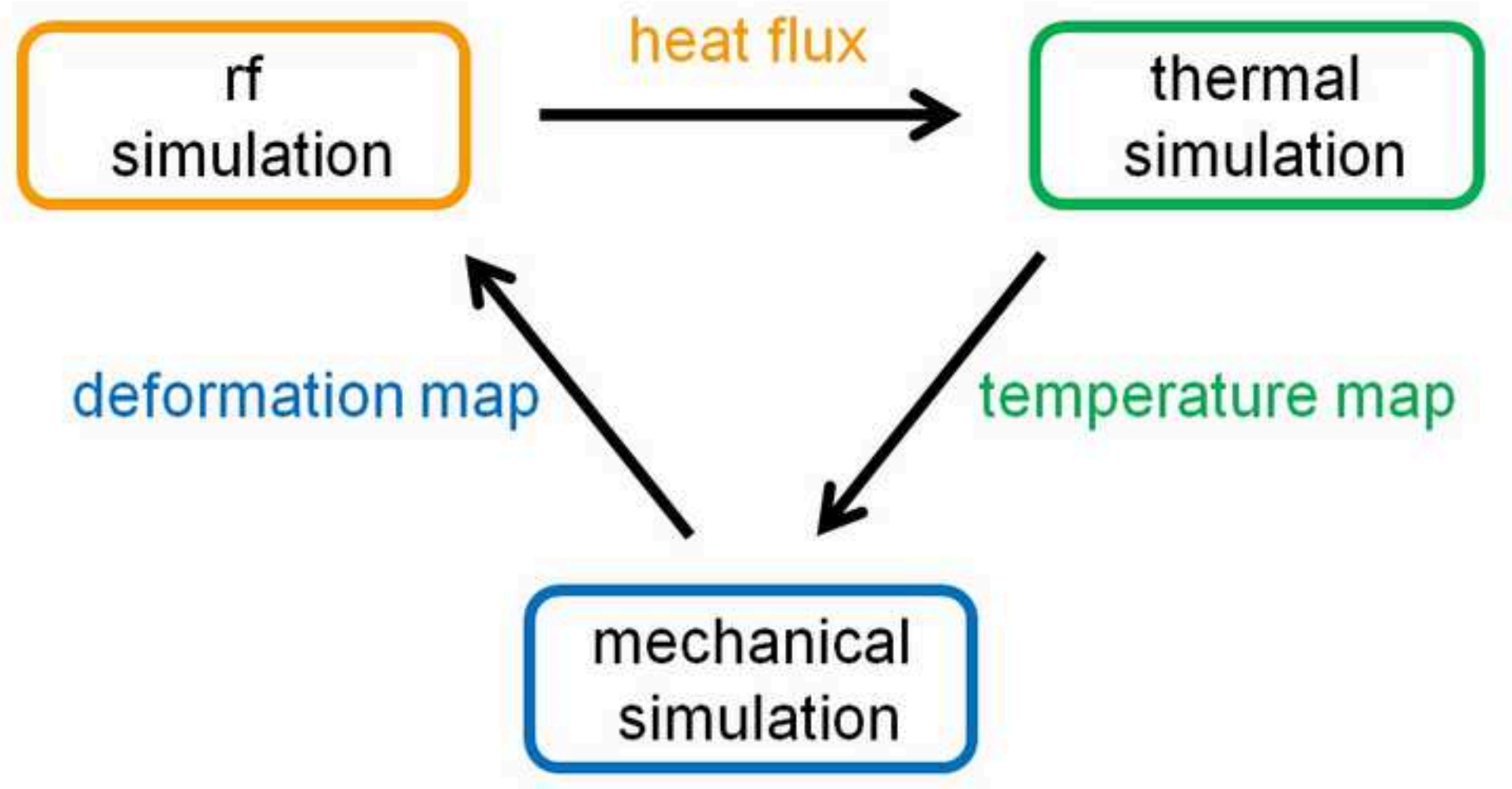

Figure 3

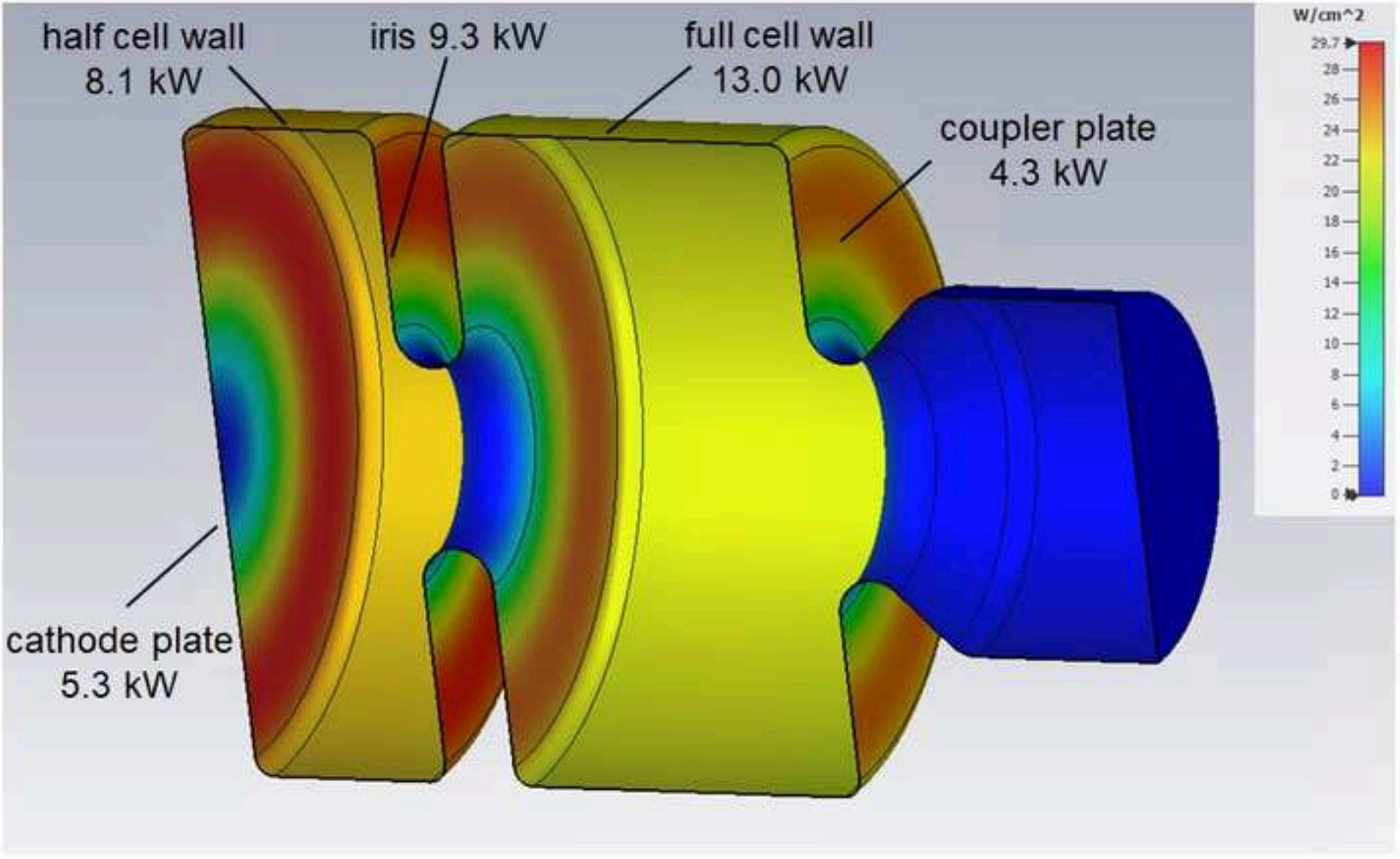

Figure 4a

Click here to access/download;Figure;Fig 4 (a).jpg

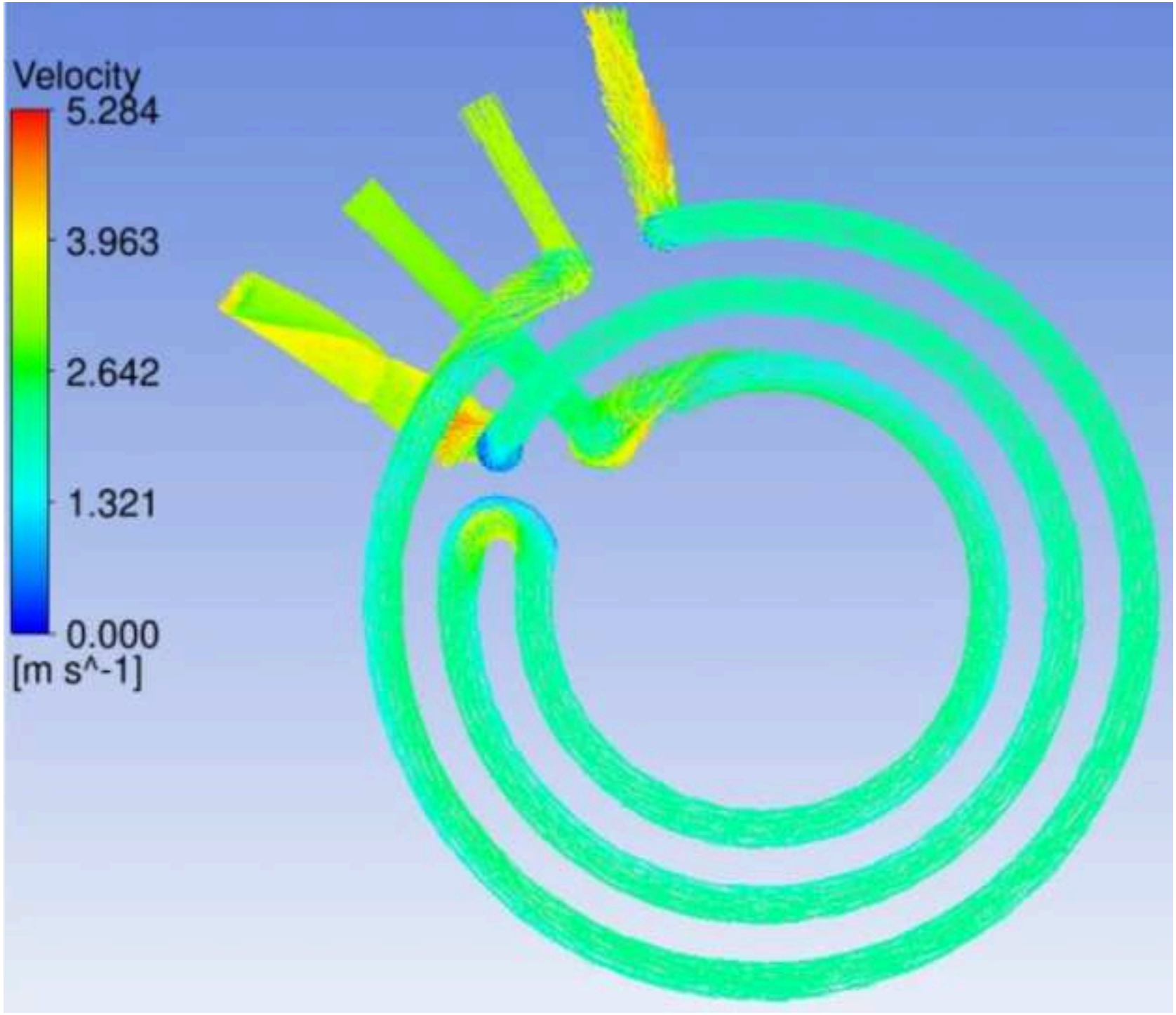

Figure 4b

Click here to access/download;Figure;Fig 4 (b).jpg

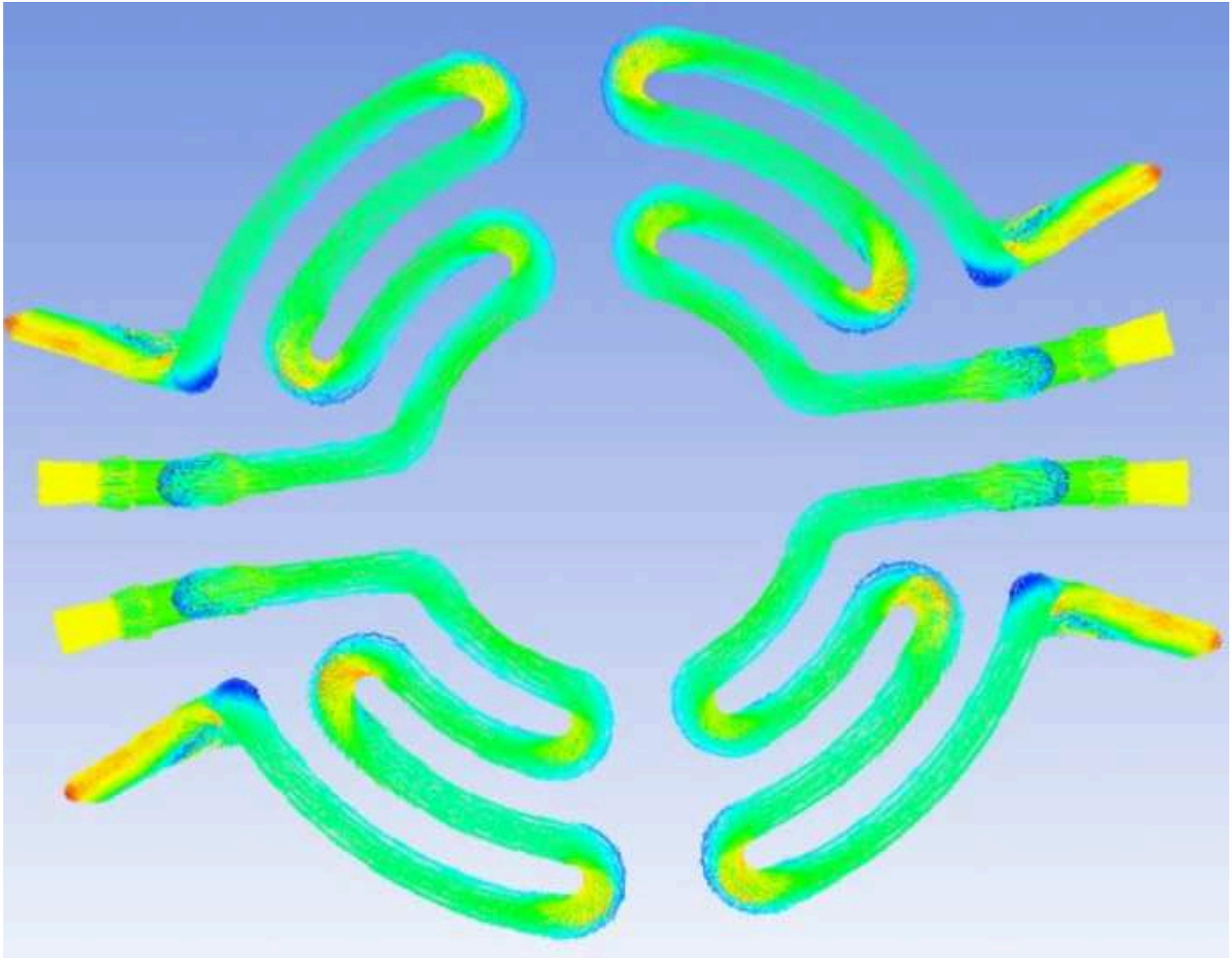

Figure 4c

Click here to access/download;Figure;Fig 4 (c).jpg

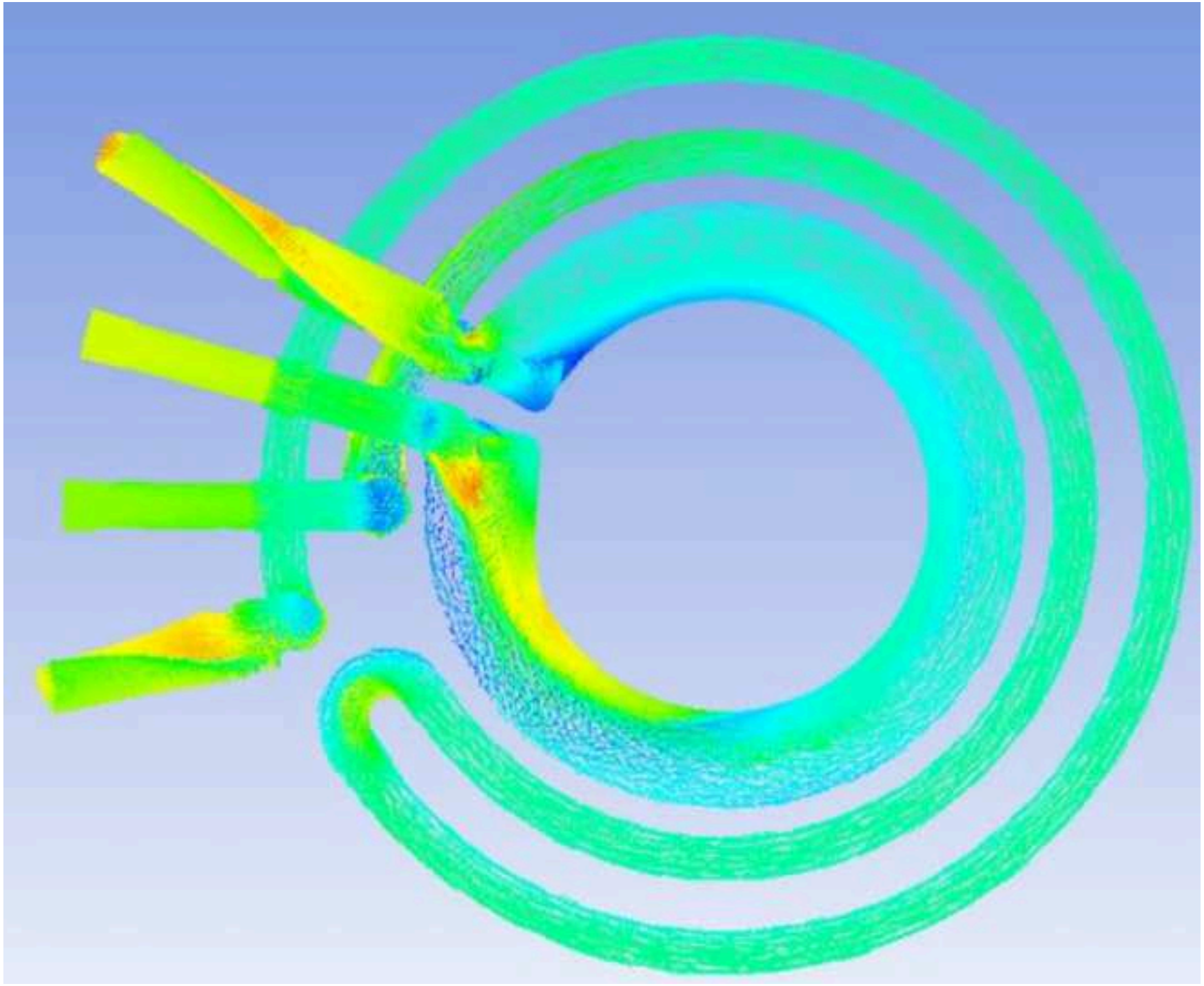

Figure 4d

Click here to access/download;Figure;Fig 4 (d).jpg

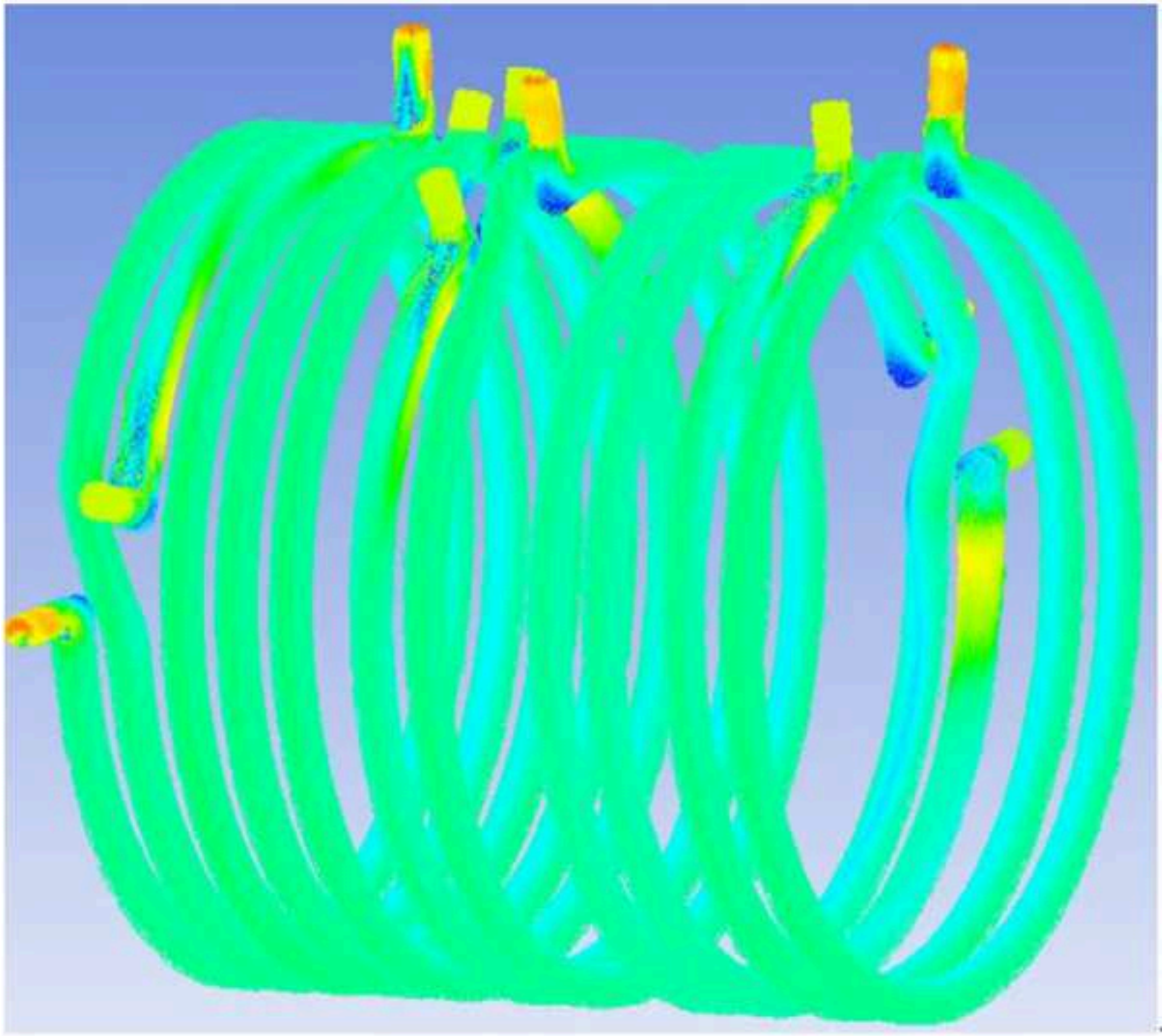

Figure 5a

Click here to access/download;Figure;Fig 5 (a).jpg

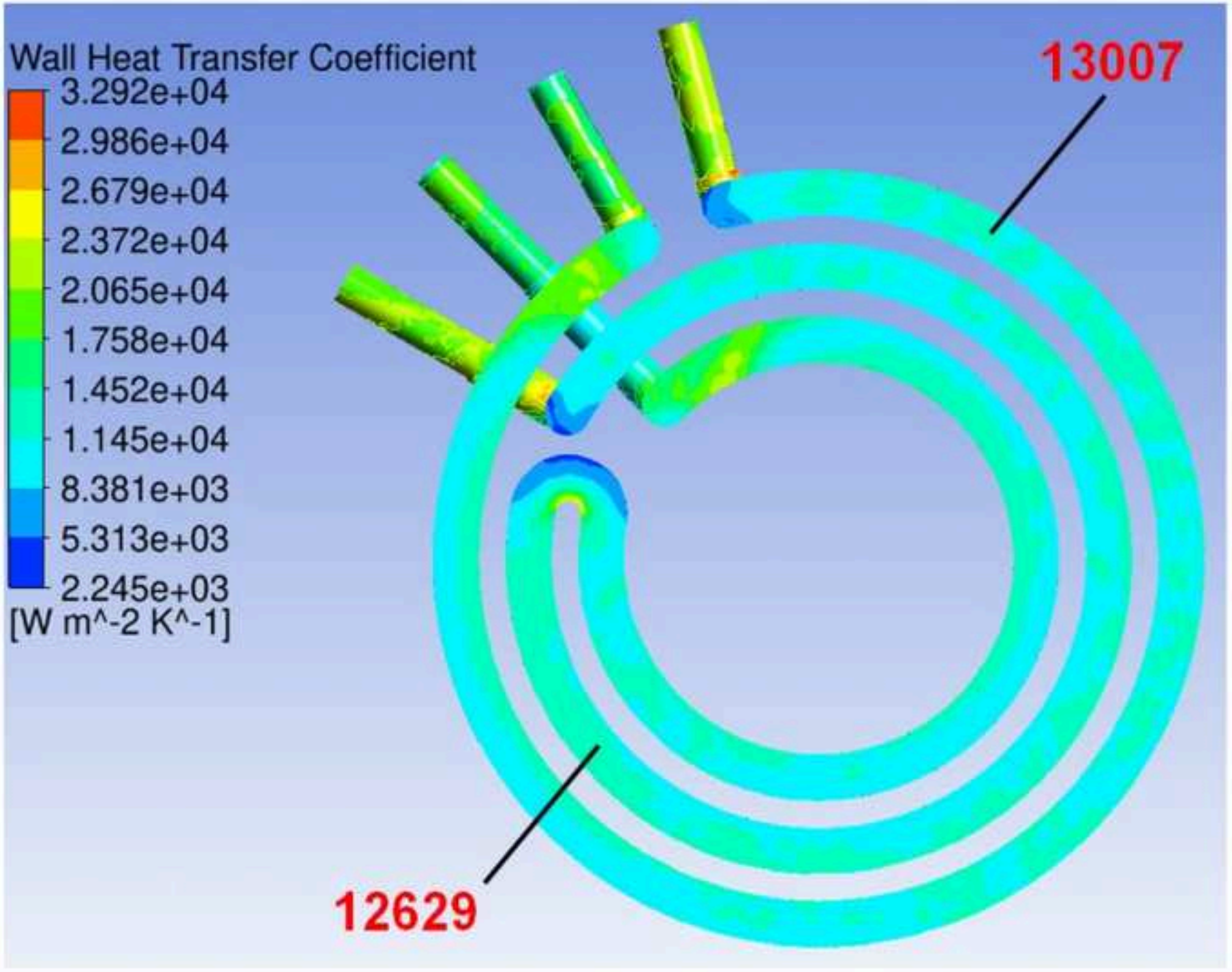

Figure 5b

Click here to access/download;Figure;Fig 5 (b).jpg

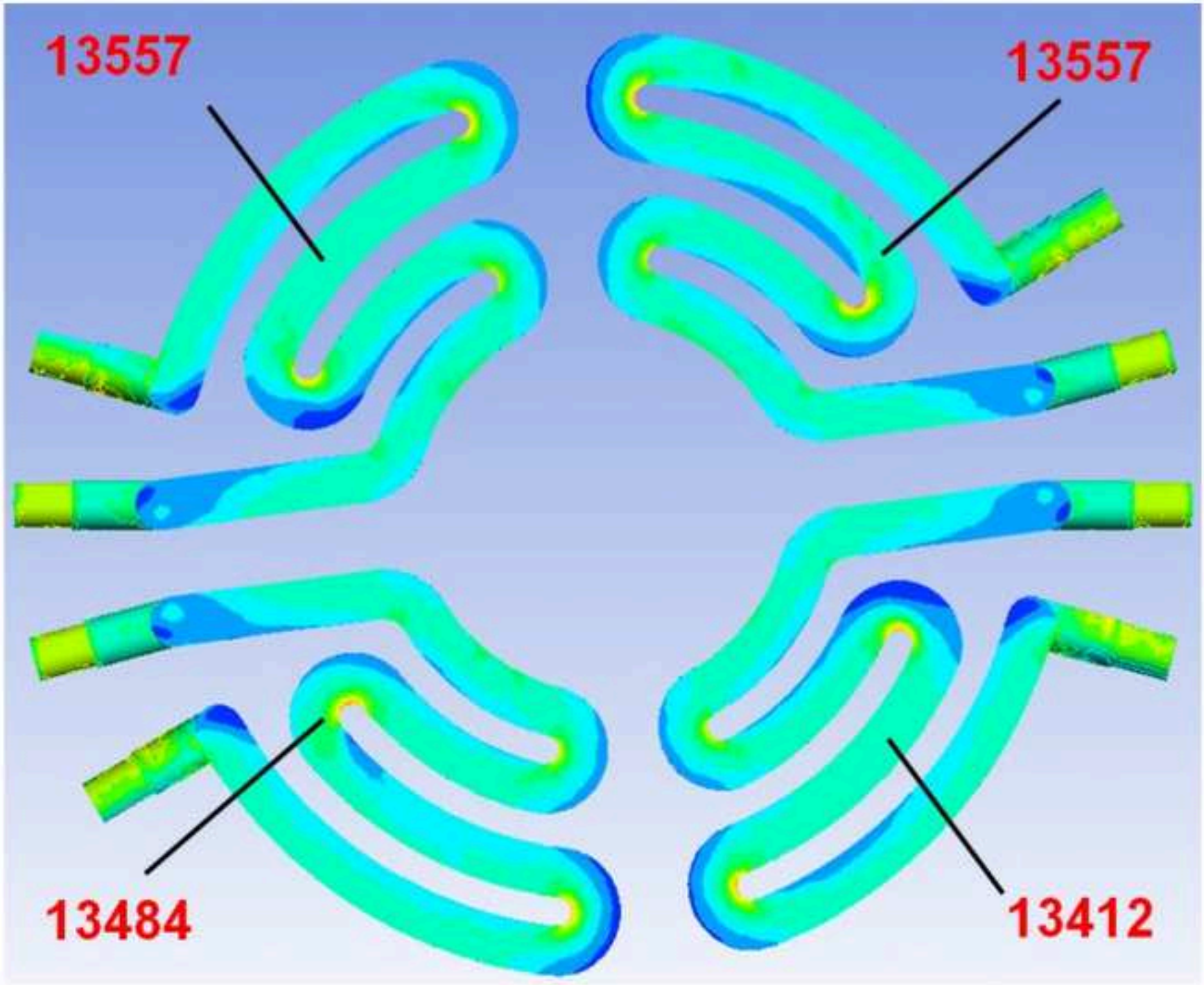

Figure 5c

Click here to access/download;Figure;Fig 5 (c).jpg

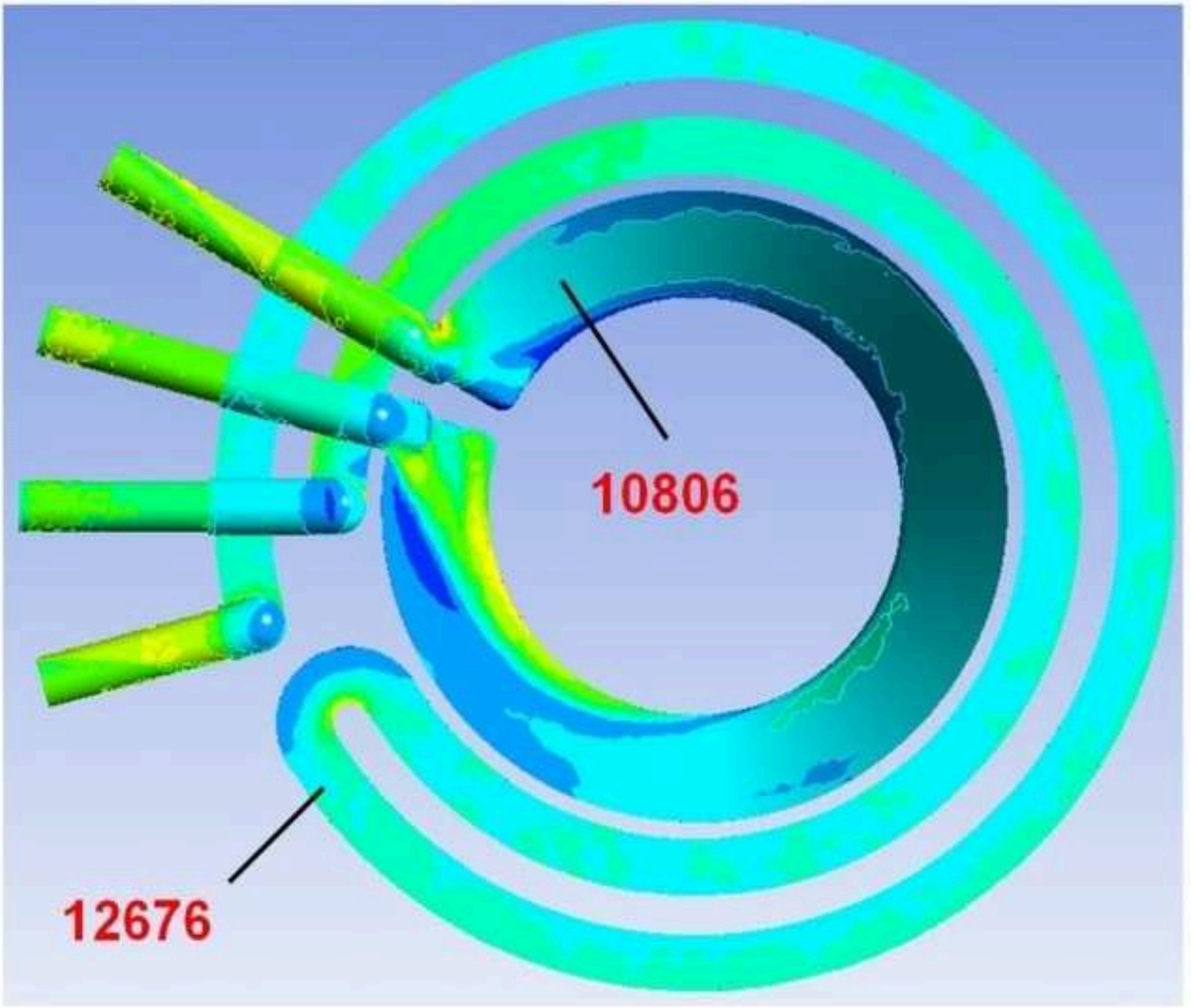

Figure 5d

Click here to access/download;Figure;Fig 5 (d).jpg

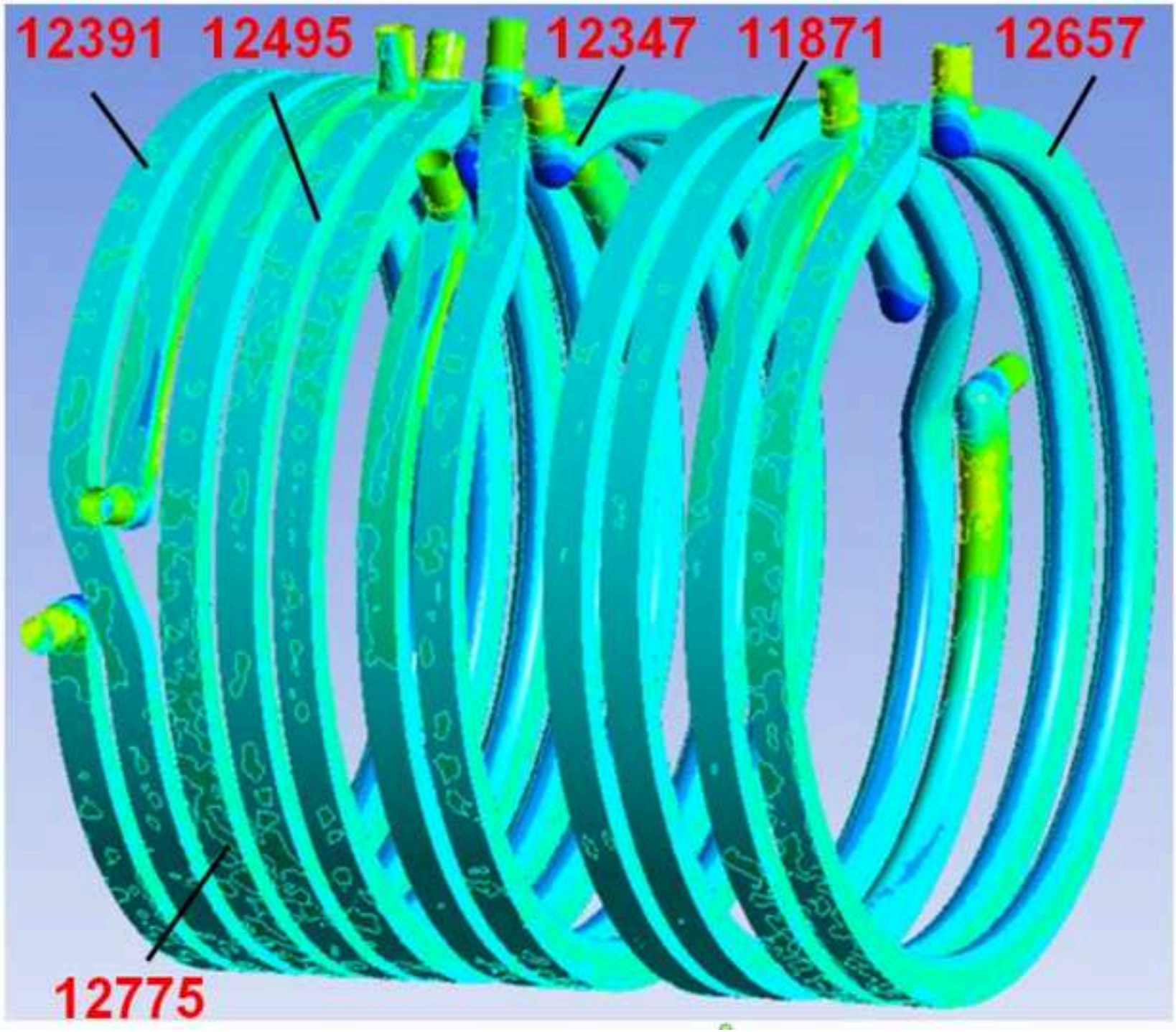

Figure 6

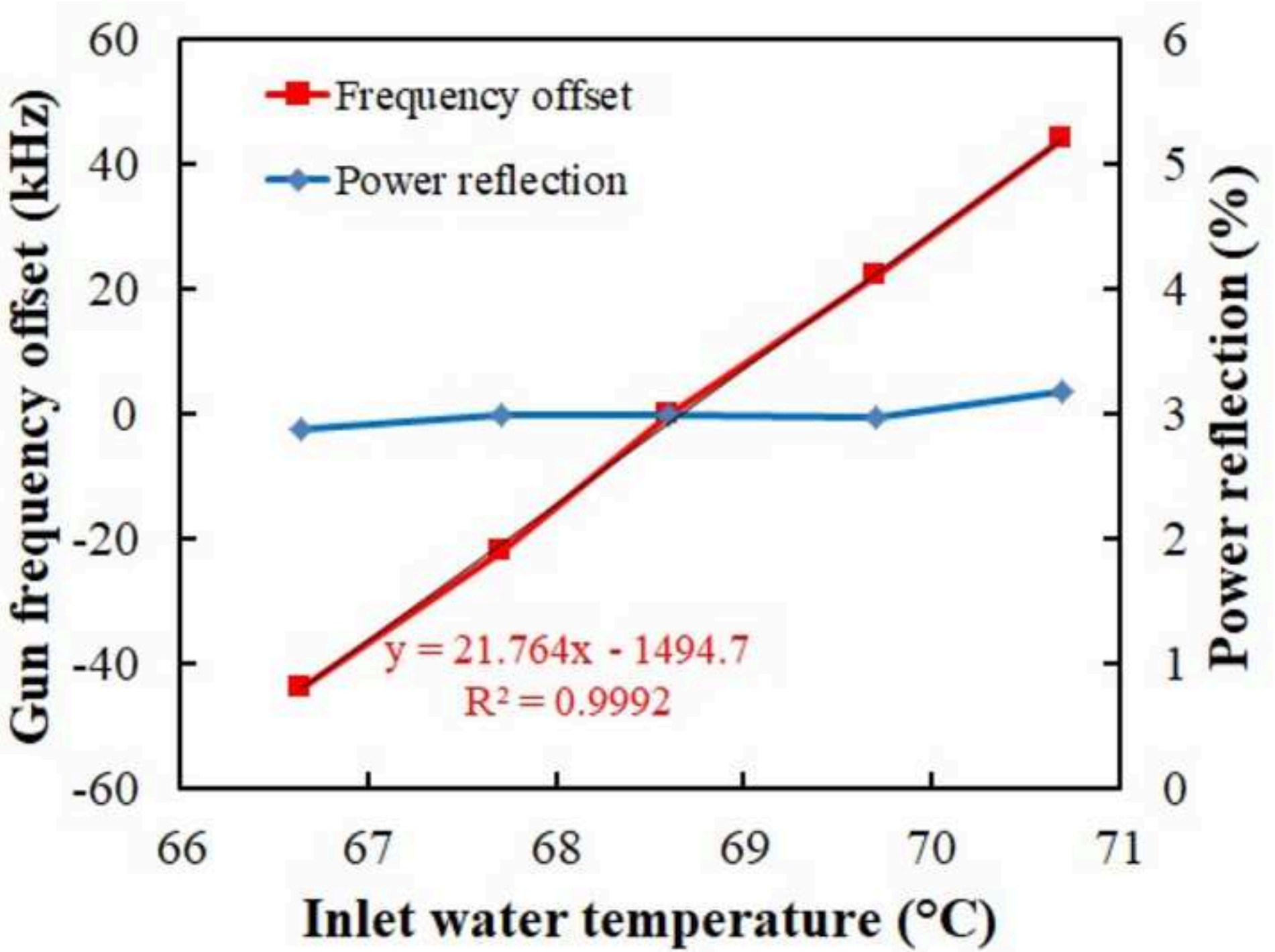

Figure 7a left

Click here to access/download;Figure;Fig 7 (a) left.jpg

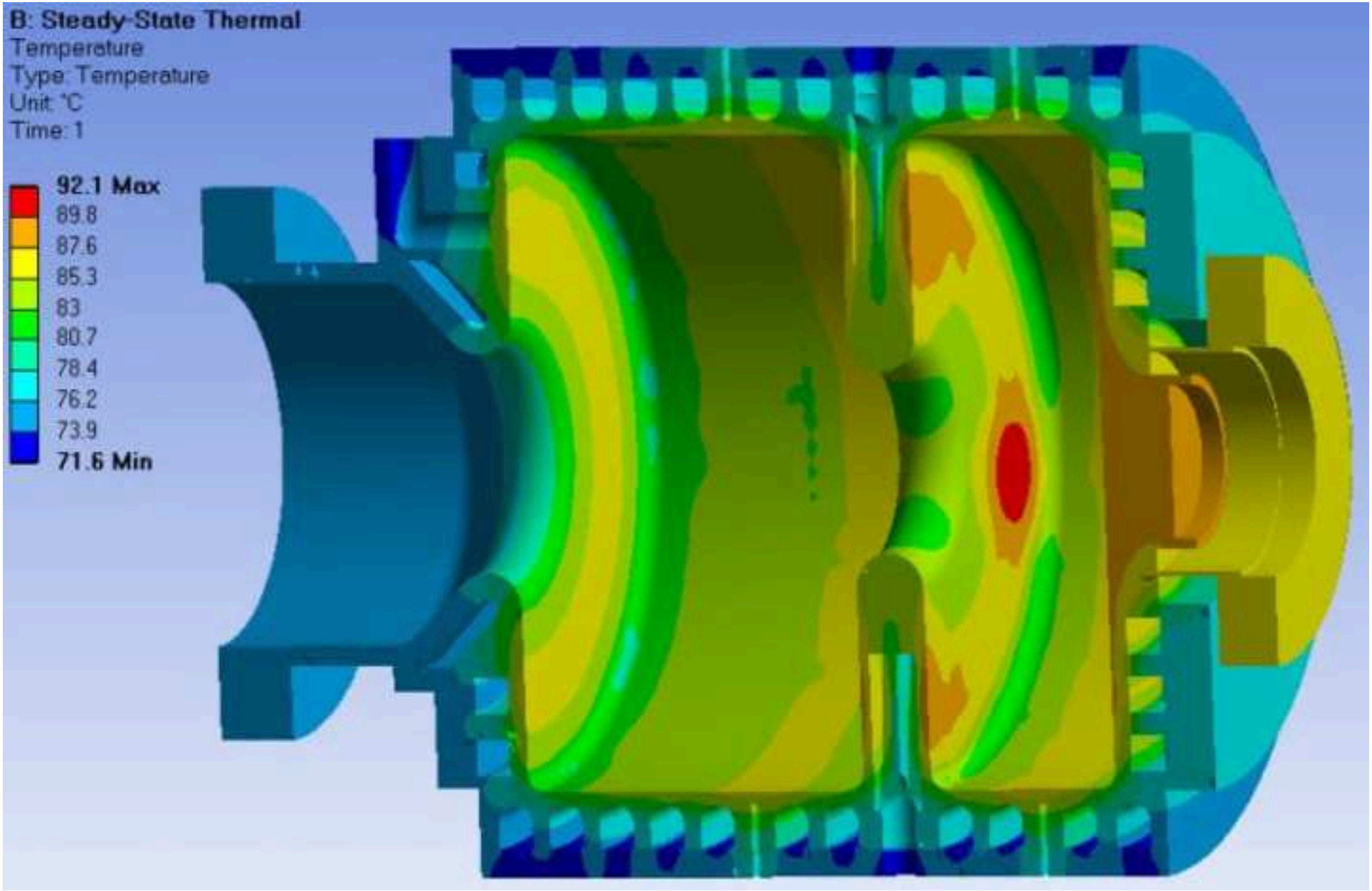

Figure 7a right

Click here to access/download;Figure;Fig 7 (a) right.jpg

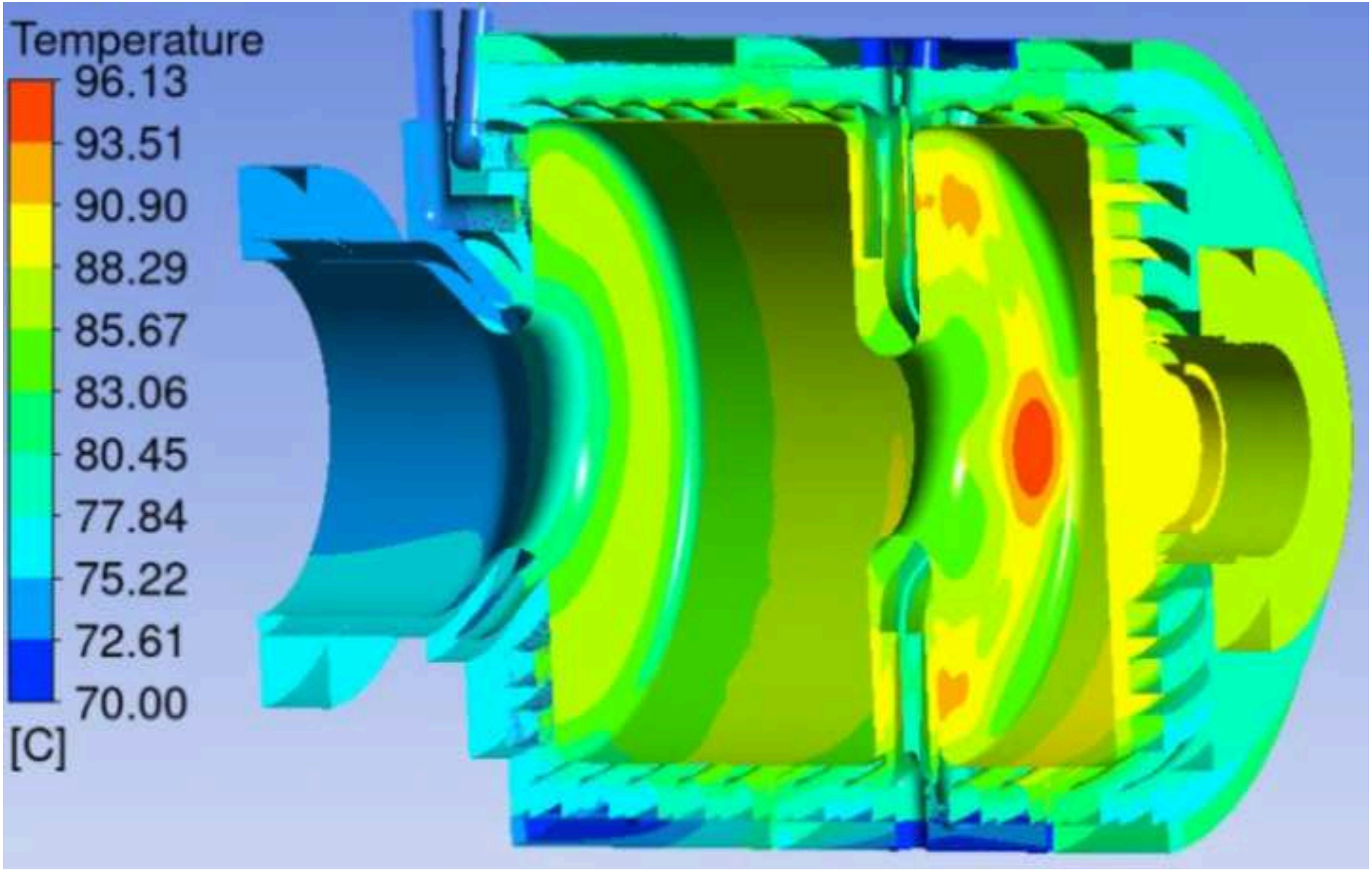

Figure 7b left

Click here to access/download;Figure;Fig 7 (b) left.jpg

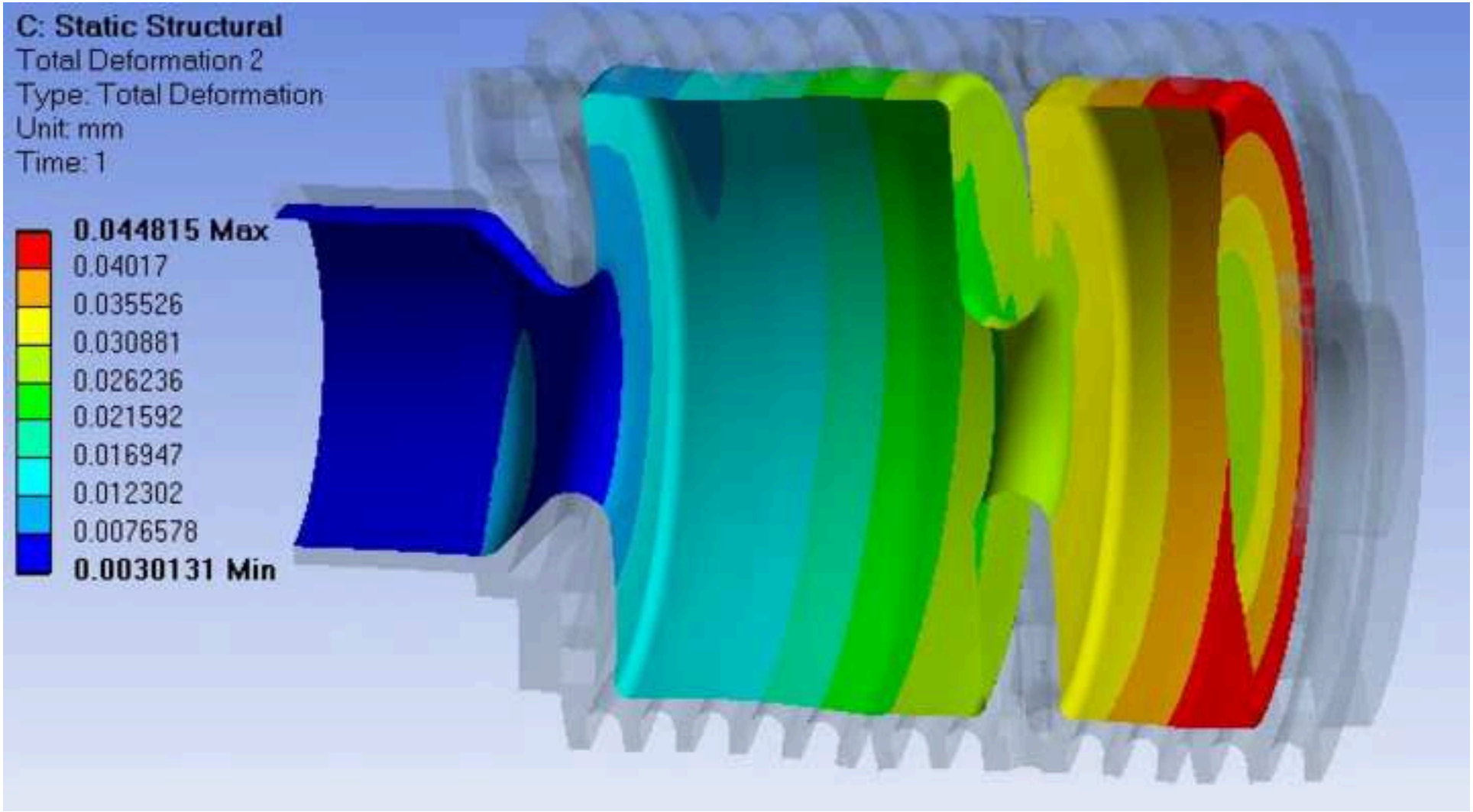

Figure 7b right

Click here to access/download;Figure;Fig 7 (b) right.jpg

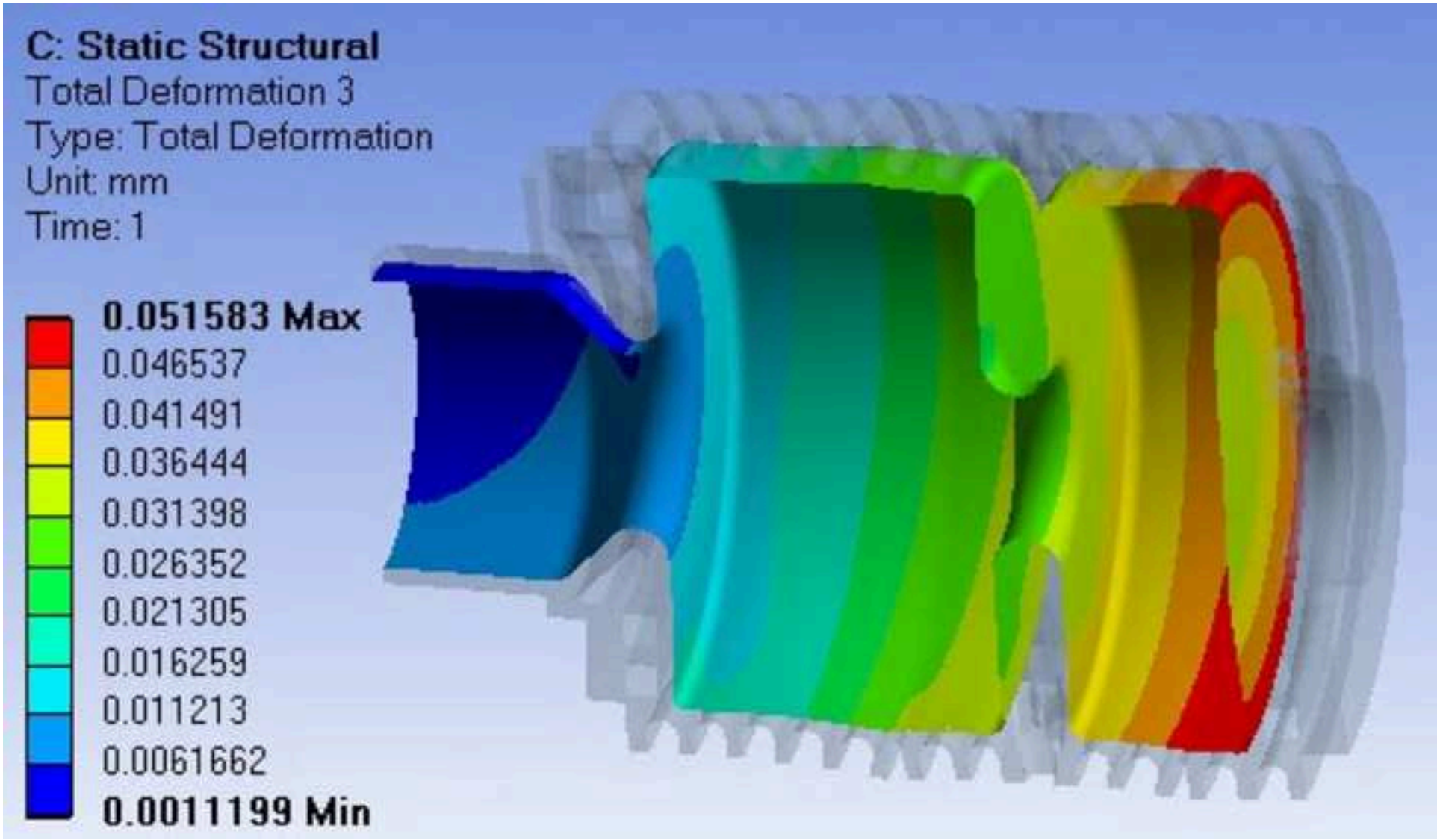

Figure 7c left

Click here to access/download;Figure;Fig 7 (c) left.jpg

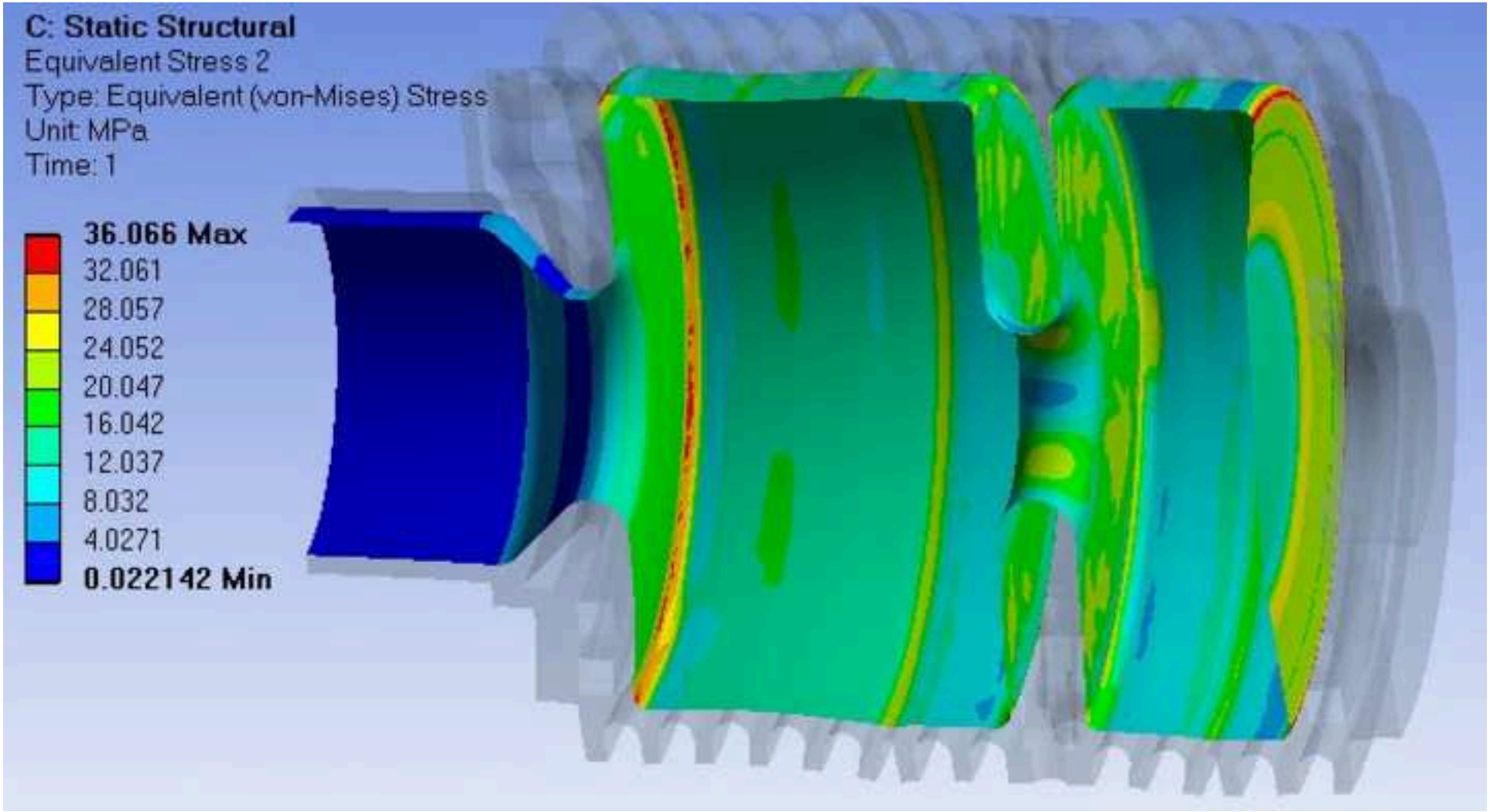

Figure 7c right

Click here to access/download;Figure;Fig 7 (c) right.jpg

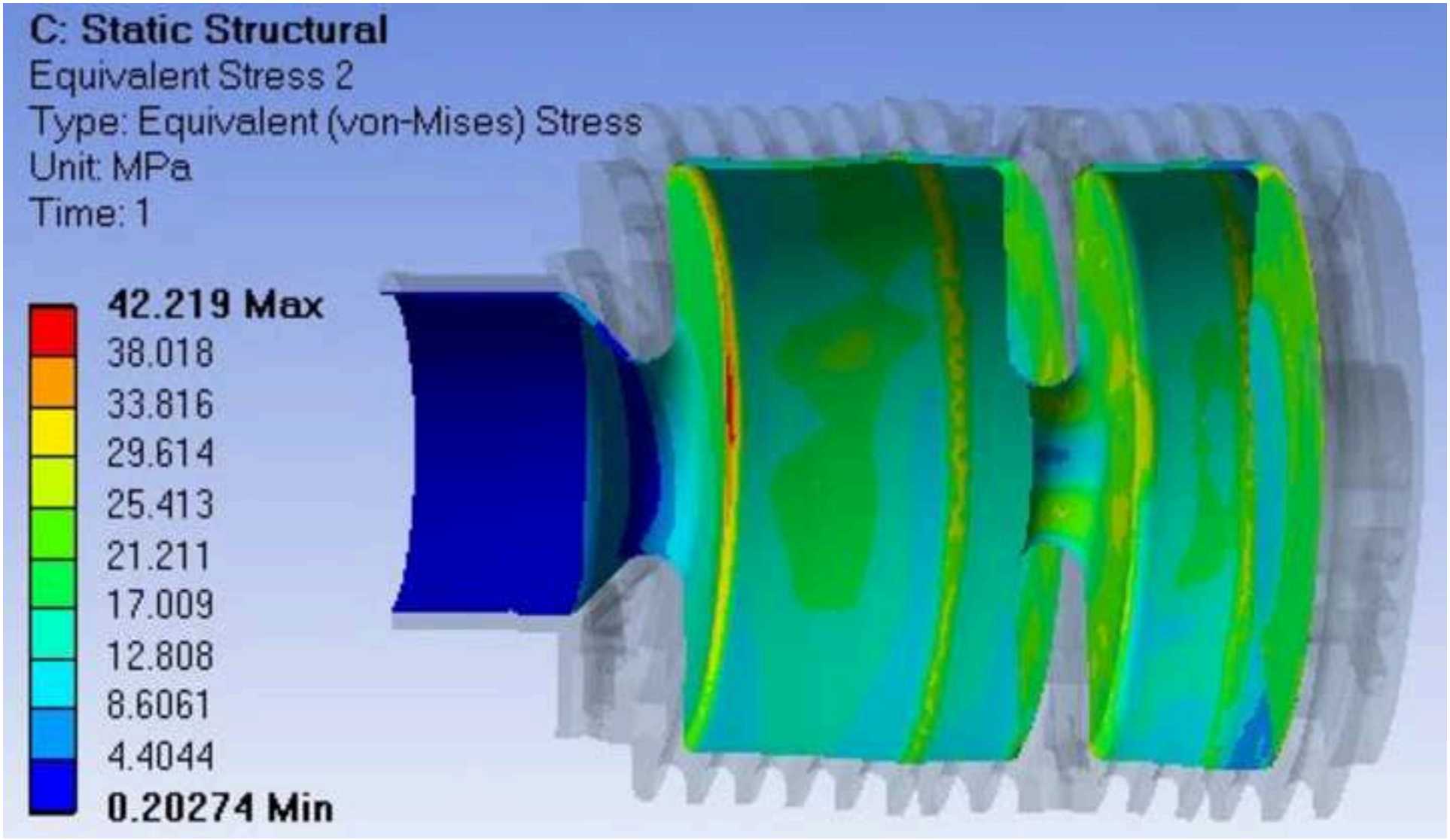

Figure 8

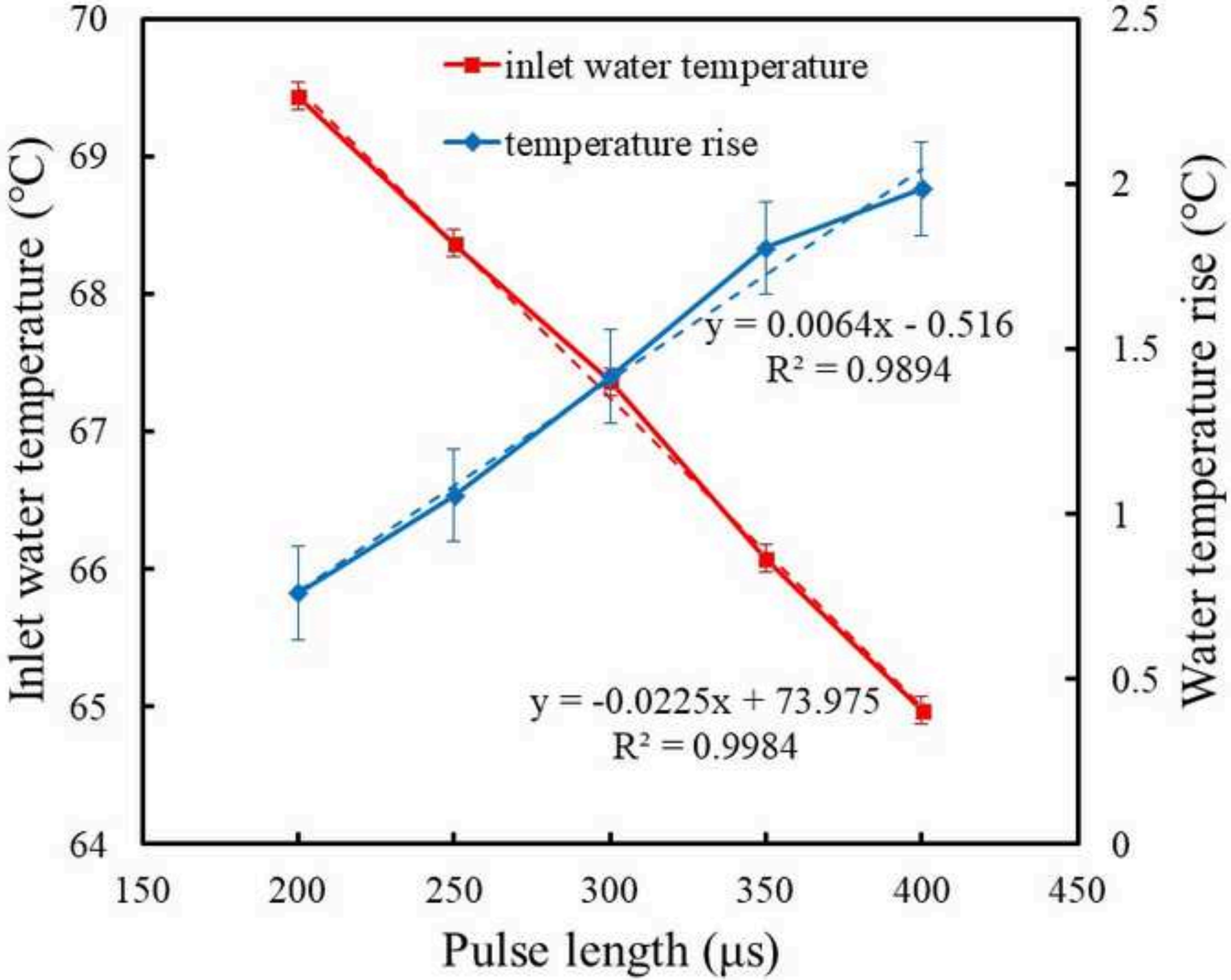

Figure 9

Click here to access/download;Figure;Fig 9.jpg

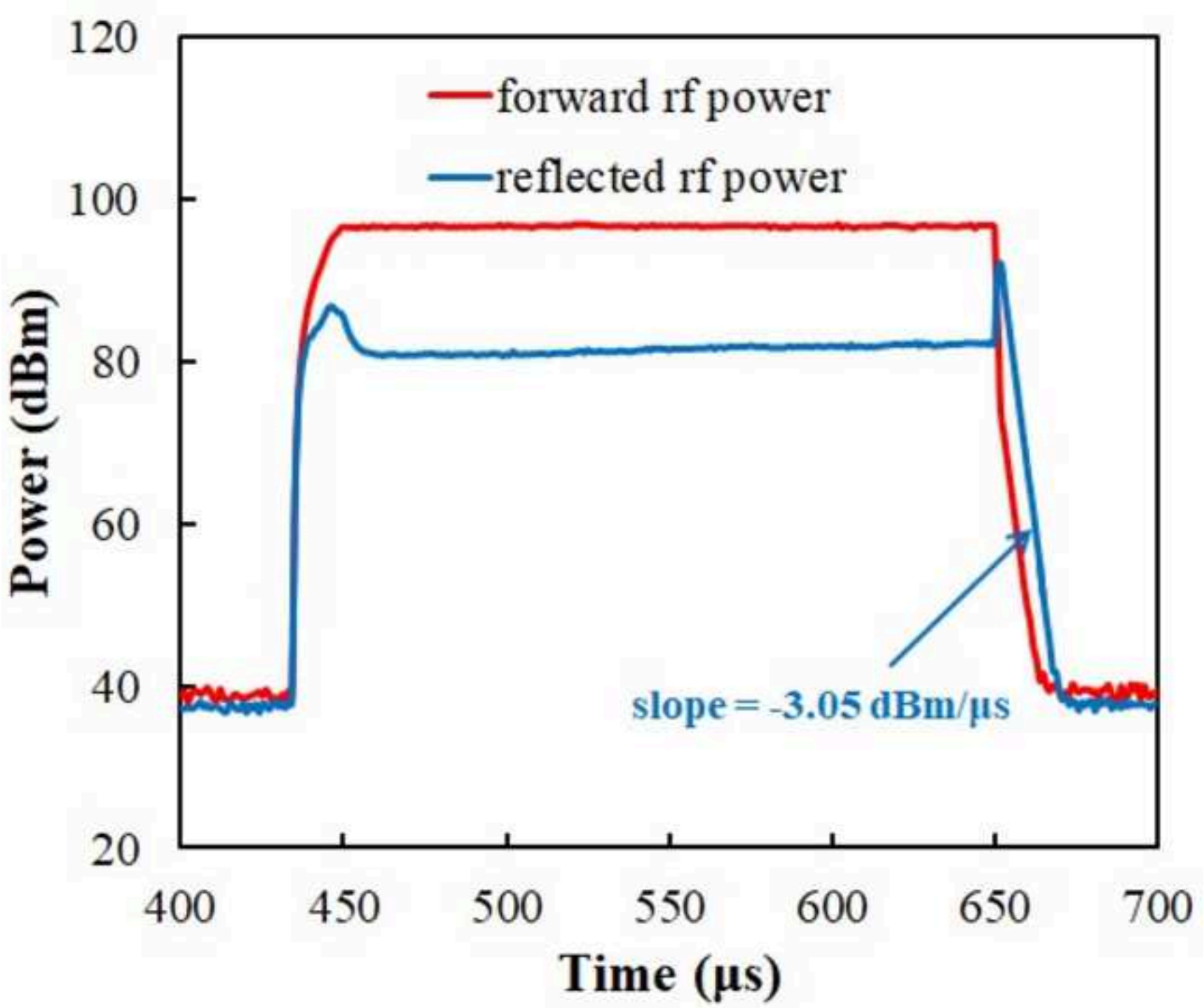

Figure 10a

Click here to access/download;Figure;Fig 10 (a).jpg

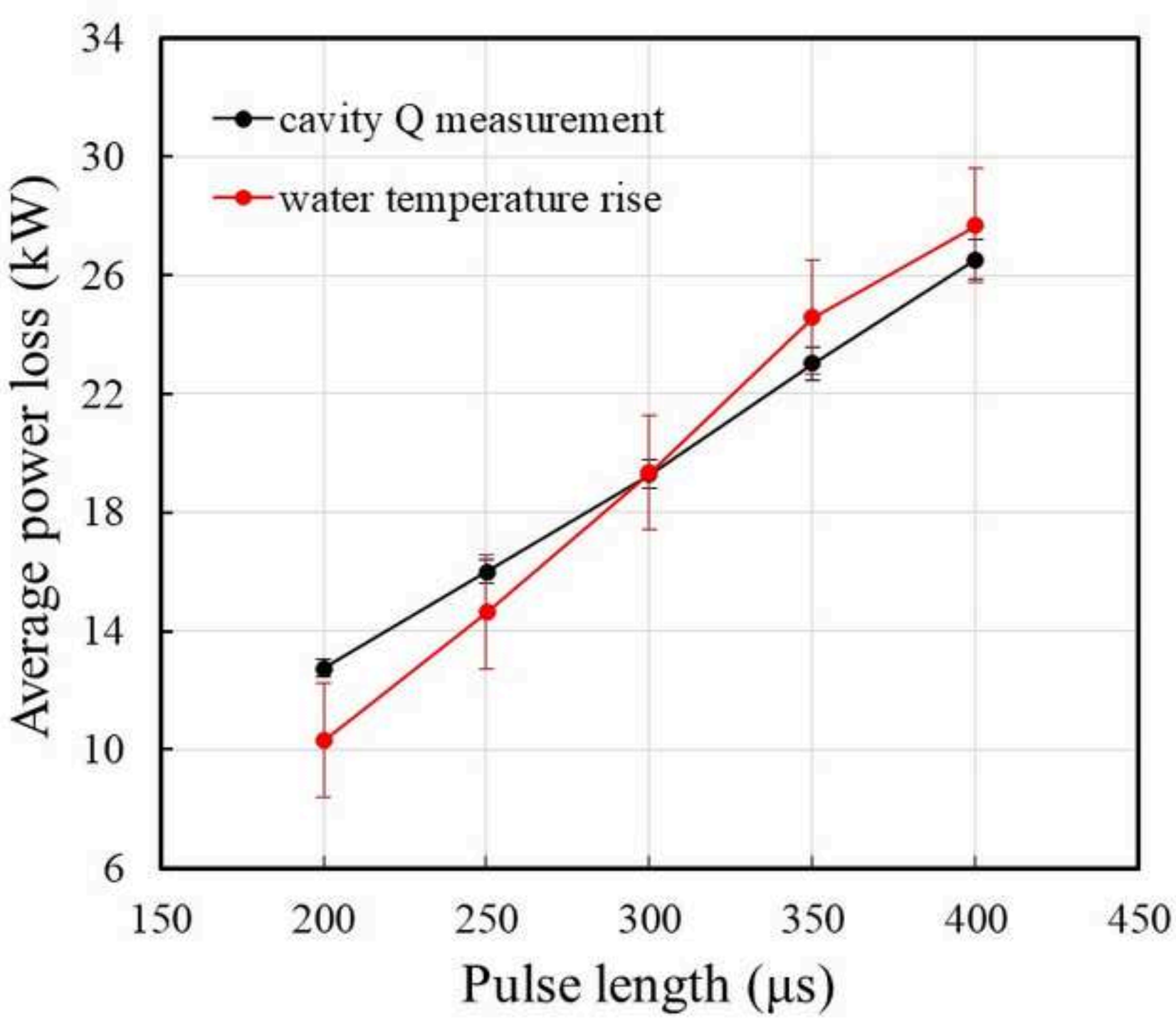

Figure 10b

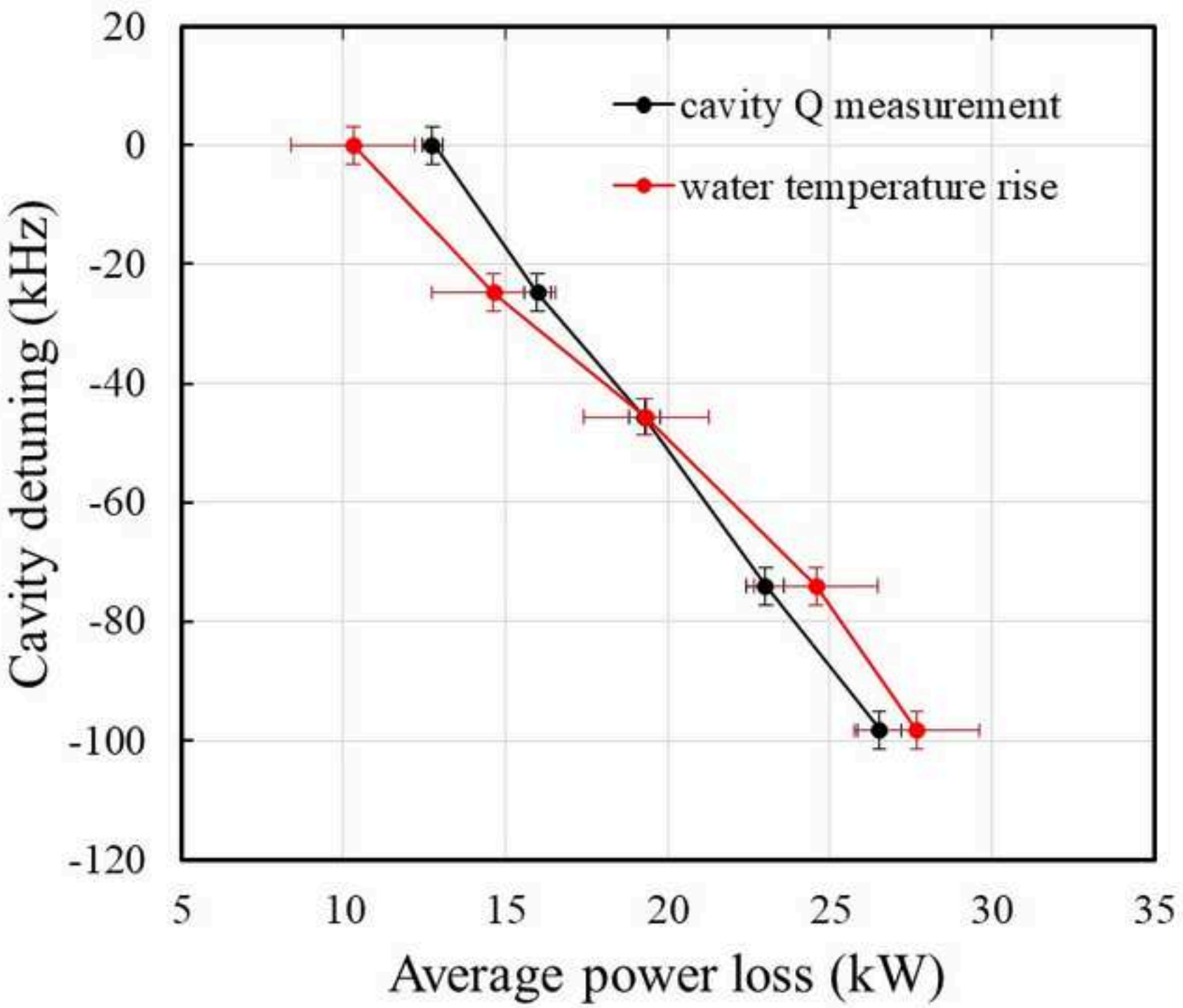

Figure 11a

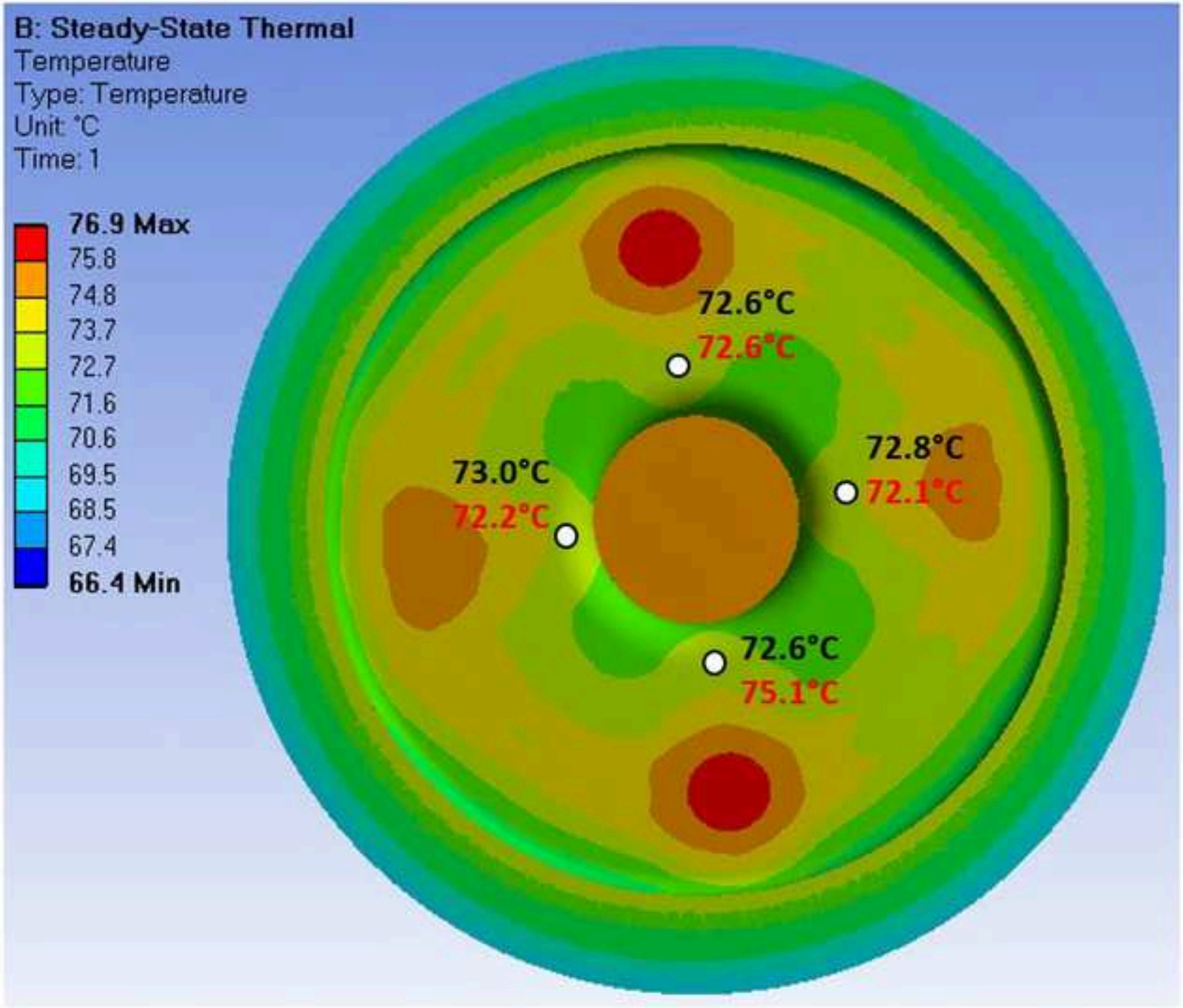

Figure 11b

Click here to access/download;Figure;Fig 11 (b).jpg

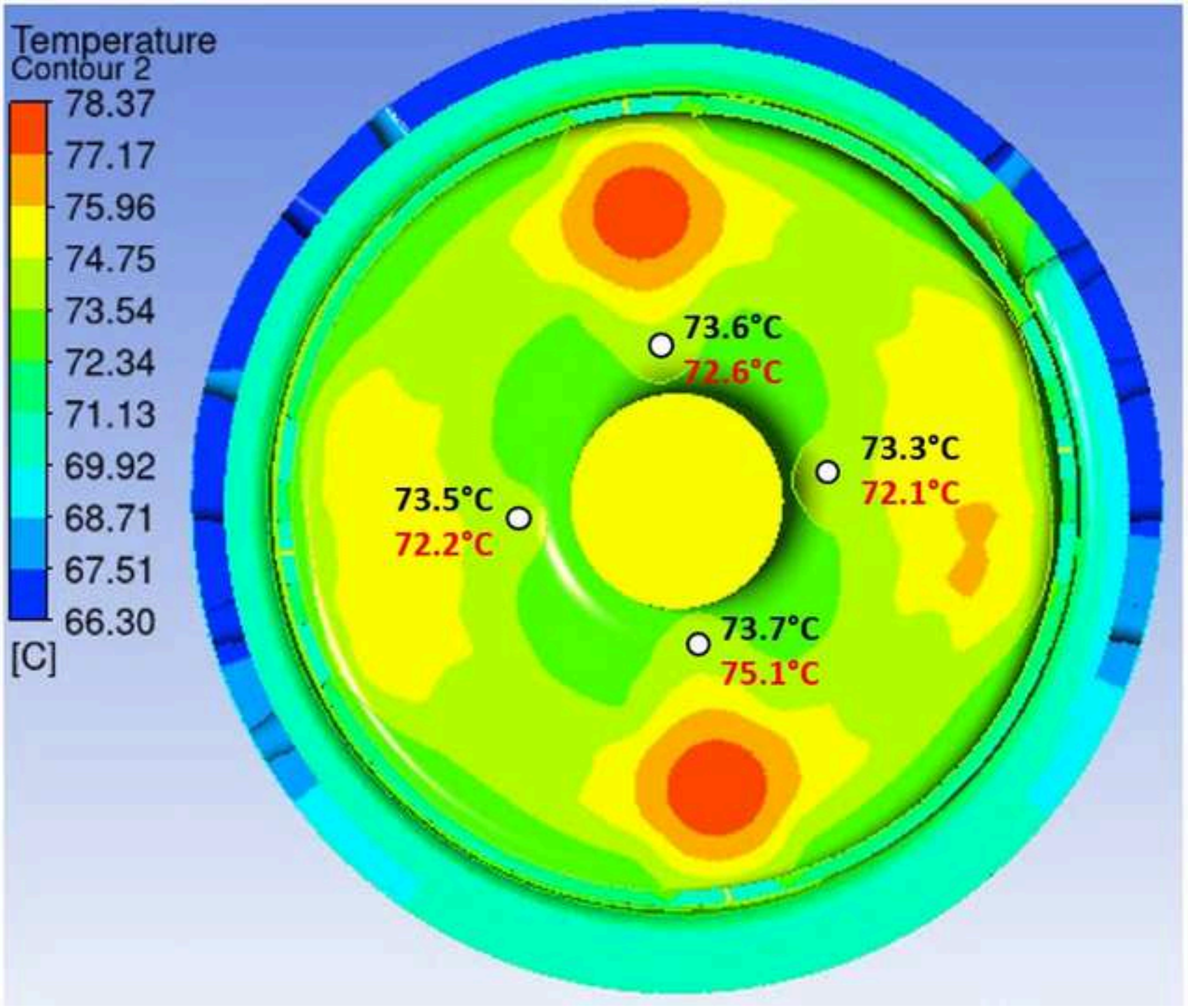

Dear reviewer,

Thanks for your comments.

Regarding your question about the boundary conditions of DESY gun 4, the explanations are following:

From Fig.1 (left), a bellow pipe exists between cathode flange and load-lock system which means the cathode flange can be expanded towards upstream. Since the constraints for gun expansion are very complicate after installing in the beam line, we tried free and fixed boundaries for approximation. Free expansion on cathode flange seems more reasonable than a sharp fixed boundary due to the bellow pipe. The simulations with free cathode flange agree with experiments as well. Therefore we use the same boundary conditions in the following section 3.3.

Some clarifications about the bellow pipe are added in line 184-185.

Best regards,

G. Shu: simulation, idea, experiment, Writing- Original draft preparation

H. Qian: idea, experiment, Writing- Original draft preparation

V. Paramonov: simulation

N. Aftab: experiment

P. Boonpornprasert: experiment

N. Chaisueb: experiment

G. Georgiev: experiment

J. Good: experiment

M. Gross: experiment

C. Koschitzki: experiment

M. Krasilnikov: experiment

A. Lueangaramwong: experiment

O. Lishilin: experiment

X. Li : experiment

S. Mohanty: experiment

R. Niemczyk: experiment

A. Oppelt: experiment

S. Philipp: mechanical discussion, mechanical drawing

F. Stephan: supervision

H. Shaker: experiment

G. Vashchenko: experiment

T. Weilbach: experiment

Declaration of interests

☒ The authors declare that they have no known competing financial interests or personal relationships that could have appeared to influence the work reported in this paper.

☐The authors declare the following financial interests/personal relationships which may be considered as potential competing interests:

Experimental benchmark study of multiphysics simulations of an L-band high average power RF gun

G. Shu [a,b,*], H. Qian [a], V. Paramonov [c], N. Aftab [a], P. Boonpornprasert [a], N. Chaisueb [a], G. Georgiev [a], J. Good [a], M. Gross [a], C. Koschitzki [a], M. Krasilnikov [a], A. Lueangaramwong [a], O. Lishilin [a], X. Li [a], S. Mohanty [a], R. Niemczyk [a], A. Oppelt [a], S. Philipp [a], F. Stephan [a], H. Shaker [a], G. Vashchenko [a], T. Weilbach [a]

[a] *Deutsches Elektronen Synchrotron DESY, Platanenallee 6, 15738 Zeuthen, Germany*

[b] *Institute of High Energy Physics, Chinese Academy of Sciences, Beijing 100049, China*

[c] *Institute for Nuclear Research of Russian Academy of Sciences, 60-th October Anniversary prospect 7a, 117312 Moscow, Russia*

Abstract

Multiphysics simulations are widely used in designing high average power RF cavities, which require iterations of RF simulation, thermal simulation and mechanical simulation in a closed loop. The reliability and accuracy of the multiphysics simulations are crucial, otherwise extra design margins are needed for simulation uncertainties. We present an experimental benchmark for the multiphysics simulations of a 40 kW L-band RF gun at the Photo Injector Test facility at DESY in Zeuthen (PITZ). The gun temperature distribution and frequency shift due to average RF heating power are measured and compared with multiphysics simulations.

Keywords: RF gun, average RF heating, multiphysics simulation, experimental benchmark.

1. Introduction

RF photoinjectors are widely used to generate high brightness electron beams for linac based free-electron laser (FEL) light sources [1-7]. The European X-ray Free-Electron Laser (European XFEL) and the Free-electron LAser in Hamburg (FLASH) are pioneers of x-ray laser generation by superconducting linac operating in the long RF pulse mode. To match the long RF pulse length (~1 ms) of the superconducting linac and beam quality requirements of an x-ray free-electron laser, the electron source is a high gradient (~60 MV/m at the cathode) L-band normal conducting RF gun operating in a long pulse mode [8, 9]. Before installing the guns at the European XFEL and FLASH sites, the guns were conditioned and characterized at the Photo Injector Test Facility at DESY in Zeuthen (PITZ) [10]. The main goal of the conditioning is to reach ~60 MV/m cathode gradient at an RF pulse duration of 650 μs and a repetition rate of 10 Hz. This corresponds to an average RF heating power of ~40 kW. In order to further increase the number of x-ray laser pulses generated in one RF pulse, an RF gun with an extended pulse length of 1 ms is requested by FLASH and European XFEL. As a consequence, the average RF heating of the gun is increased by 50% to 60 kW. To meet this challenge, a new generation of RF gun with several improvements was designed, and the first prototype is under fabrication [11]. One of the main improvements is the gun water channel optimization aiming for increased cooling capabilty.

For the high average RF power cavity, water cooling circuit design is essential to reduce overheating, thermal stress and resonant frequency dependence on the RF power. Multiphysics simulations are widely used to verify and optimize the cavity designs, e.g. continuous-wave (CW) radio frequency quadrupole (RFQ) [12], CW buncher [13, 14] and RF gun [11, 15, 16]. With advances of the modern simulation codes and computing power, multiphysics problems of higher complexity can be simulated, which is of vital importance to achieve a reliable simulation result. Results should converge as a sequence of mesh density. Besides, the self-consistent simulations of heat exchange in cooling channels and proper boundary constraints of mechanical structures are critical for reliable simulation of RF heating effects. In the worst case, an unreliable multiphysics simulation may significantly underestimate the RF heating effect, i.e. the cavity temperature rise, the frequency shift and the cavity thermal stress, which will lead to bad vacuum, insufficient frequency tuner range and shorter cavity lifetime. Therefore, multiphysics simulations of RF heating effects are benchmarked with the experiments in this paper.

To benchmark the RF cavity heating effect, measurements of cooling water temperature rise, cavity temperature rise and cavity frequency shift are straightforward, while the measurements of cavity deformation and thermal stress are more difficult. An example of the experimental benchmark study was performed for an RFQ at Japan Atomic Energy Agency (JAEA) [17] with a two-

*guan.shu@desy.de

dimensional approximate analysis. In the simulations, the average temperature of inlet and outlet water was used as the constant cooling temperature, and the heat exchange for vane and wall channels were derived by fitting the measured inlet and outlet water temperature rises. Finally, the 2D simulations reproduced the measured cavity frequency response to water temperature and RF heating. Another benchmark example for DESY gun was presented in Ref. [18, 19]. The heat transfer coefficients based on the empirical equations were used in the 3D simulations. This is an engineering approach which assumes a uniform cooling channel and homogenous water speed in the channel cross section. The simulated iris temperature rise was ~20% underestimated compared to the measured value. Later on, the heat transfer coefficient distribution simulated by the computational fluid dynamics (CFD) software was adopted in the RF cavity design [20]. Unlike the uniform distribution derived from the empirical approach, the simulated heat transfer coefficient between water and cavity reflects the nonuniform distributions of water flow speed and cooling channel dimensions. Since the simulated heat transfer coefficient is more close to the cooling channel reality than the engineering approach, it is more precise to describe the heat exchange between cavity and cooling water. For example, it was adopted in the thermal simulations of the latest 60 kW DESY gun [11] and the 400 Hz S-band RF gun at STFC Daresbury Laboratory [20].

In this paper, an experimental benchmark of multiphysics simulations for the DESY 40 kW L-band normal conducting RF gun is presented. The paper is organized as follows. In Section 2, a brief description of the gun system is presented. Section 3 illustrates the detailed numerical simulations of the gun. In Section 4, the high power experimental procedures, results and error analysis are reported. The comparison between simulations and measurement results are shown. Section 5 gives a brief discussion on the usage of multiphysics simulations in designing an RF cavity.

2. Brief introduction to the DESY L-band normal conducting RF gun

The DESY L-band RF gun of 4th generation (Gun 4) consists of a 1.6 cell copper cavity surrounded by a stainless steel jacket. The schematic view of the gun is shown in Fig. 1. The cathode plug is inserted into the cavity backplane through a load lock system without breaking the vacuum. The RF power is fed into the cavity from a 10 MW multi-beam klystron via a hollow waveguide (WR-650) to a 'doorknob' type coaxial coupler. The gun is normally conditioned up to a peak power of ~6 MW at a pulse duration of 650 μs and a repetition rate of 10 Hz, corresponding to a ~6 MeV beam with a peak acceleration field of ~60 MV/m at the cathode. The maximum average RF power dissipated in the cavity is up to ~40 kW. The gun has implemented 14 cooling channels (see Fig. 1) for heat removal and resonance control. The water channel distributions are arranged according to the surface heat flux distribution aiming for a high heat transport efficiency and a uniform temperature distribution. The latter one is meant to reduce the temperature gradient in the cavity body hence a smaller structure stress. Each channel is equipped with a water flow meter allowing monitoring and control of the water flow. Numerous temperature sensors are mounted to record the gun body and cooling water temperatures. One of the temperature sensors inside the gun central iris disk serves for the water temperature feedback system for stable operation. The cavity frequency tuning at various average power levels is realized by adjusting the inlet water temperature while the water flow is kept constant. The water flow velocity in the cooling channels is ~2 m/sec, and the total water consumption is ~12 m^3/h in routine operation.

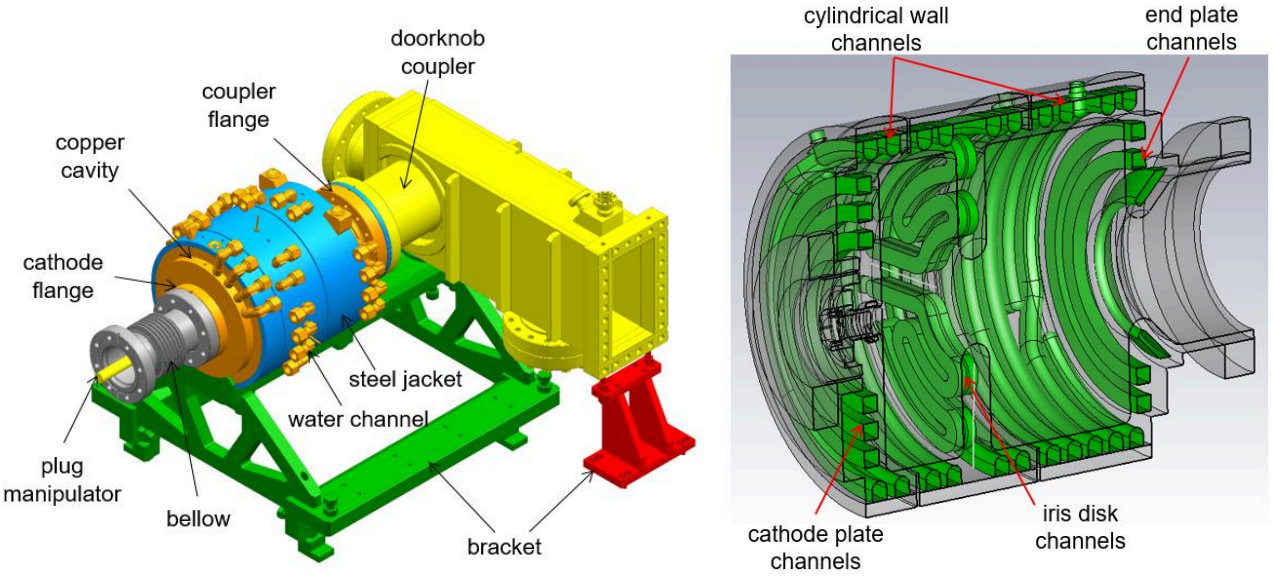

Fig. 1. Schematic view of the DESY Gun 4 assembly (left) and cooling channel distributions (right).

3. Multiphysics analysis of the RF gun

Since the RF gun operates in a long pulse mode, both the average RF heating and pulsed heating effect are of paramount importance for the long term operation reliability and stability. The details about the pulsed heating analysis can be found in Ref. [21, 22]. The measurements and the benchmark simulations in this paper focus on the average RF heating effect. The material properties used in the simulations are listed in Table 1. The mechanical analysis adopts the linear elastic modulus because the maximum stress under a power level of 40 kW in the following simulations is less than the yield strength limit of the material.

Table 1. Material parameters of the gun body in the simulations.

Parameters	OFHC copper	Stainless steel
Thermal conductivity [W/m/K]	391	16.3
Thermal expansion coefficient [1/K]	1.67×10^{-5}	1.59×10^{-5}
Young's modulus [GPa]	123	193
Poisson ratio	0.345	0.28
Electrical conductivity [S/m]	5.8×10^{7}	N/A

3.1 Multiphysics simulation methodology

The multiphysics simulations comprise the integrated electromagnetic, thermal and mechanical simulations, as shown in Fig. 2. The RF simulations were performed by using CST MICROWAVE STUDIO (CST MWS) version 2019 [23], and the thermal and mechanical simulations were conducted by CST MULTIPHYSICS STUDIO (CST MPS) [23]. The coupled simulations were also carried out with ANSYS workbench version 20.1 [24] for comparison.

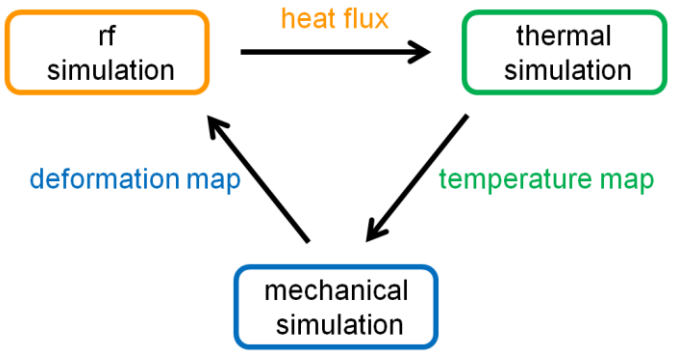

Fig. 2. Schematic workflow of the multiphysics simulations.

The RF simulation was first initiated to obtain the field distribution of the resonant π mode, thereby calculating an initial resonance frequency. The heat flux generated by RF field is determined by the surface magnetic field strength, which can be described as [25]:

$$P_c = \frac{1}{2}\sqrt{\frac{\pi f_0 \mu_0}{\sigma}}|H_t|^2 \quad (1)$$

where f_0 denotes cavity frequency, μ_0 is the vacuum permeability, σ is the electric conductivity of copper and H_t is the inner surface magnetic field amplitude. The internal surface power loss density distribution simulated by CST MWS is shown in Fig. 3. When the total power loss is scaled to 40 kW, the maximum thermal loss density is 29.7 W/cm^2. The RF simulations with ANSYS gave a similar power loss distribution.

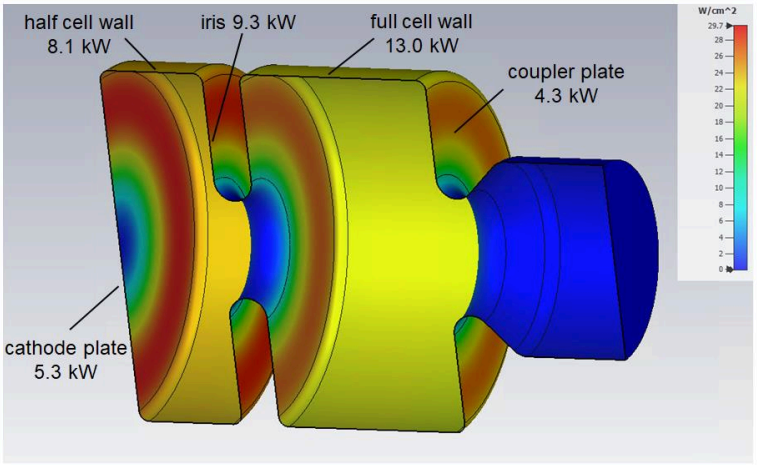

Fig. 3. Surface power loss density distribution with a total power loss of 40 kW (simulated by CST MWS).

Then, the heat flux map is transferred to the thermal module to evaluate the steady-state temperature distribution. The heat exchange between water and cavity plays a significant role in the temperature simulation and the following cavity deformation and frequency shift. Therefore, it must be precisely defined in the thermal analysis. Two options are usually used for the heat transfer coefficient calculation: an empirical equation and fluid dynamics simulations.

The empirical heat transfer coefficient α can be expressed as [26]:

$$\alpha = \lambda \cdot Nu/d \tag{2}$$

where λ is the thermal conductivity of the water, Nu is the dimensionless Nusselt number and d is the hydraulic diameter which is calculated from the area and wetted perimeter of the flow cross-section.

A criterion for turbulent water flow in a water tube is given by the Reynolds number [26]:

$$Re = \frac{V_m \cdot d}{\nu} \tag{3}$$

where V_m is the fluent velocity and ν is the kinematic viscosity. The water in the Gun 4 is in the turbulent regime (Re $\geq$ 10000) and Nu can be calculated by [26]:

$$Nu = 0.023 \cdot Re^{0.8} \cdot Pr^{0.4} \tag{4}$$

$$Pr = \frac{\eta C_p}{\lambda} \tag{5}$$

where Pr is the Prandtl number, η is the dynamic viscosity and C_p denotes the specific heat capacity of the fluid. The fluent velocity in one channel can be calculated from the flow rate and the cross-section area. Both CST MPS and ANSYS can do thermal simulations by using the empirical heat transfer coefficient. The water temperature at the water-pipe interface is assumed to be constant, not considering the water temperature rise along the cooling channel. The average temperature of inlet and outlet water is used in the simulations as an approximation. Besides, the heat transfer coefficients in one channel are assumed to be constant, not considering water velocity changes near the corners.

For a heavy heat loaded cavity with complex cooling channels like the Gun 4, the fluid dynamics simulation via ANSYS CFX code is more close to reality and therefore preferred. The variations of water temperature and flow velocity in the cooling channels can be reflected in the simulations, providing more precise heat exchange compared to simplified calculations based on empirical formulas. The simulation results are shown in Fig. 4 and 5. The average water speed in the channels is ~2 m/s. Due to the channel inhomogeneity, the size of the inlet and outlet cylindrical pipe is smaller than the rest part leading to a relatively higher local water speed as well as a higher local heat transfer coefficient. The water speed near the 180° bend outer corner vicinity is slow (less than 1 m/s). As a result, the surface heat transfer factor in this vicinity is only ~30% of the average value of the whole channel. The empirical heat transfer factor of each channel is 10~20% higher than the average value simulated by CFX (see Fig. 5). The detailed cavity temperature distributions with these two calculation methods are presented in the following sections.

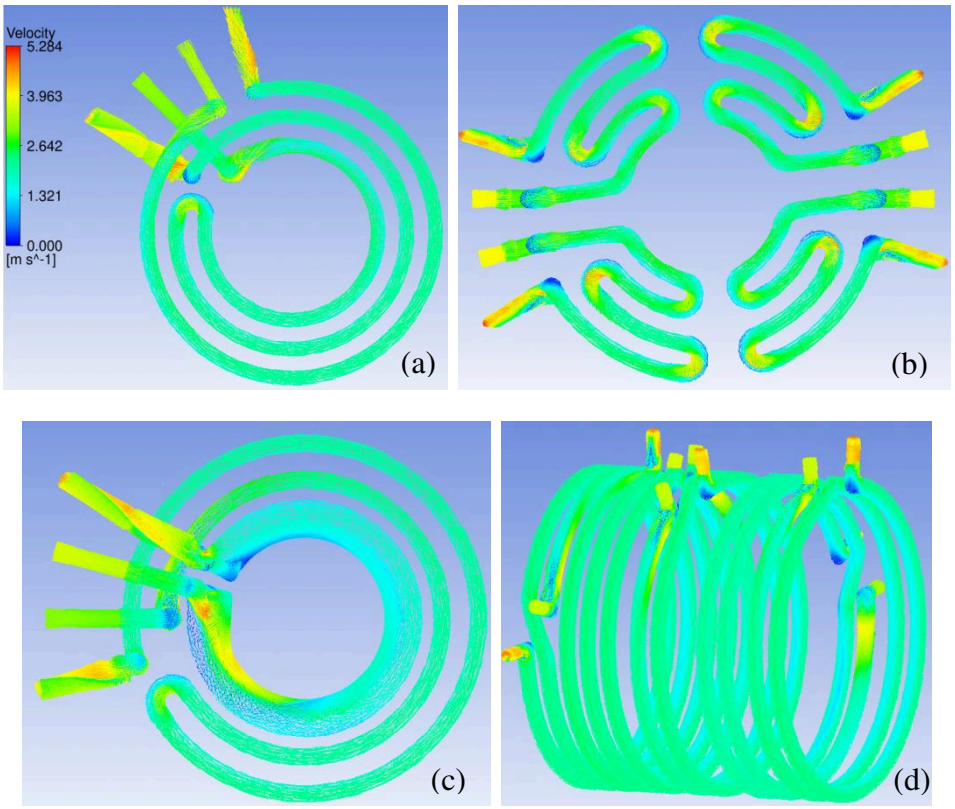

Fig. 4. Simulated water speed distributions by using the flow rate in operation (12 m^3/h total water flow): flow velocity in the channels of (a) cathode plate, (b) iris disk, (c) end plate, (d) cylindrical wall.

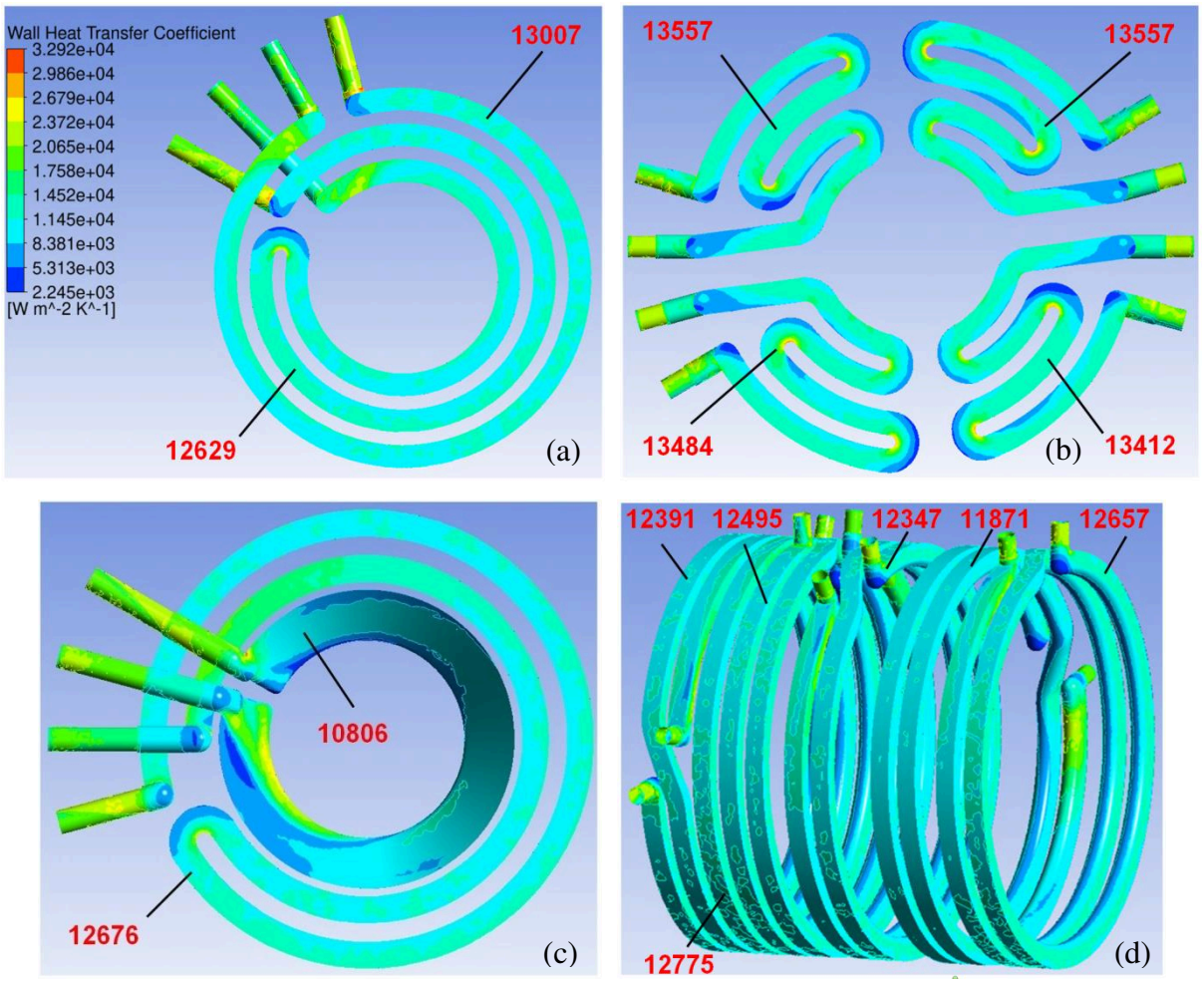

Fig. 5. Simulated heat transfer coefficient distributions in the channels of (a) cathode plate, (b) iris disk, (c) end plate, (d) cylindrical wall. The cooling conditions in operation (~70°C water temperature and 12 m^3/h total water flow) were used in simulations. The numbers in red represent the empirical calculation for comparison.

For the mechanical simulation, the cavity deformation is evaluated based on the thermal expansion coefficient of the material and the temperature rise w.r.t the reference value. The induced stress depends on the temperature gradient, material properties and cavity geometry shape. Besides, the boundary constraints of the structure will also affect the deformation distributions and therefore structure stress and cavity frequency shift, so the boundary constraints should be defined as realistically as possible.

In the last step, the resonant frequency is calculated again with the deformed shape in the RF simulations to estimate the resonant frequency shift.

During the coupled simulations, the mesh quality in each module and the mesh matching between modules are also critical for reliable results. It is necessary to find a proper mesh definition by a mesh convergence study. In the benchmark simulations, the total mesh cell number in each module is in several million scales.

3.2 Water temperature effect on the gun frequency

Since no mechanical frequency tuners exist in the RF gun, the water temperature is used for tuning the cavity frequency at various RF heating loads. In the free expansion approximation, the relationship between frequency shift Δf and temperature change ΔT is:

$$\Delta f = \alpha f_0 \Delta T \tag{6}$$

where α is the material thermal expansion coefficient shown in Table 1, f_0 is the operating frequency1300 MHz. The gun consists of a copper cavity surrounded by a stainless steel jacket. Since the thermal expansion coefficients of copper and steel are not identical, the theoretical temperature detuning sensitivity is in the range of 20.7 - 21.7 kHz/°C. Once the gun is installed in the beamline, the expansion with external constraints is difficult to be calculated analytically due to the complex external constraints. Therefore measurements were performed at PITZ to study the gun frequency dependence on cooling water temperature. A feed-forward phase modulation was implemented in the low level RF (LLRF) system allowing us to adjust the klystron output frequency within the klystron bandwidth. The frequency offset was scanned to match the gun resonant frequency, and thus minimizing the reflected power. Therefore, the gun frequency shift at various water temperatures can be tracked. In the measurements, the gun was fed swith a 200 μs and 10 Hz RF pulse with a peak power of 4.8 MW. The corresponding average RF power loss was ~10 kW. The inlet water temperature was scanned in a range of 4°C. The dependence of gun frequency shift on the inlet water temperature is shown in Fig. 6. The water temperature detuning sensitivity was measured to be 21.8 kHz/°C.

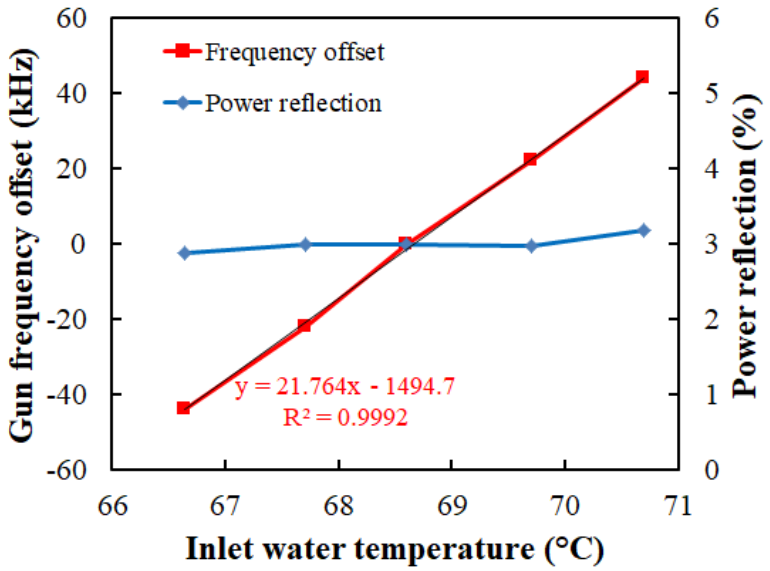

Fig. 6. Forward RF frequency offset w.r.t. 1300 MHz versus different inlet water temperature. For each temperature, the gun forward peak power was kept at 4.8 MW and the power reflection was kept at 3%.

In the benchmark simulations, we considered two possible mechanical boundary conditions. One is the longitudinally fixed boundary only on the coupler flange (see Fig. 1), considering a hard constraint from the coupler waveguide and a negligible soft constraint from the cathode flange with a bellow. The other one is the longitudinally fixed constraints on both the coupler side and the cathode flange. The first boundary setting indicates similar features as free boundaries. The gravity was not included in the simulations due to its relatively small cavity weight.

Table 2. Water temperature effect on gun frequency with different boundaries and software.

	Longitudinally fixed at coupler flange	Longitudinally fixed at coupler and cathode flange
CST [kHz/°C]	21.2	28.1
ANSYS [kHz/°C]	21.2	28.3

Table 2 summarizes the simulation results of the water temperature effect on gun frequency. A high-quality mesh was generated in both codes based on the mesh convergence study. As a consequence, the CST result agrees well with ANSYS. The longitudinally fixed constraint at the coupler flange proves to be closer to the measurements. Free expansion of the cathode flange is a reasonable assumption due to the bellow between cathode flange and load-lock system (see Fig. 1). Therefore, the same boundary was applied to the model in the following mechanical simulations.

3.3 Average RF heating effect

An inlet water temperature of 70°C was set as the reference temperature in the thermal and mechanical simulations, and the average power dissipated on the inner surface was set to 40 kW. The cavity heat removal is accomplished through air and water cooling. The free convection between gun and air is typical ~5 W/(m^2·K) which implies little influence on the thermal conduction. The water flow measured in each channel was used to calculate the heat transfer coefficient. In the thermal simulation with empirical heat transfer coefficient, the water temperature rise between inlet and outlet water was included. The average water temperature rise was calculated to be 2.9°C based on the 40 kW power dissipation and the 12 m^3/h water flow. Then, the average value of inlet water and outlet water temperature was applied to the cooling channels. The distributions of temperature, deformation and stress by using empirical and ANSYS CFX simulated heat transfer coefficients are shown in Fig. 7.

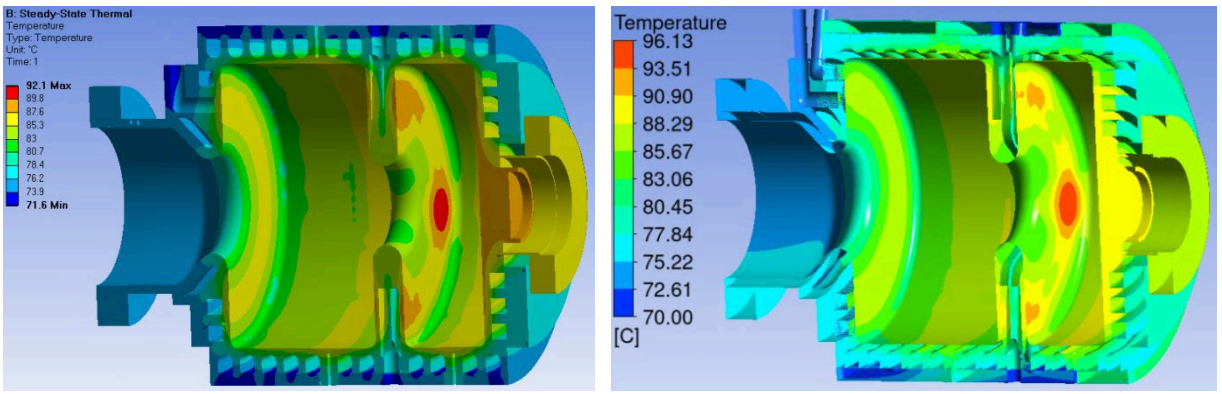

(a) gun temperature distribution

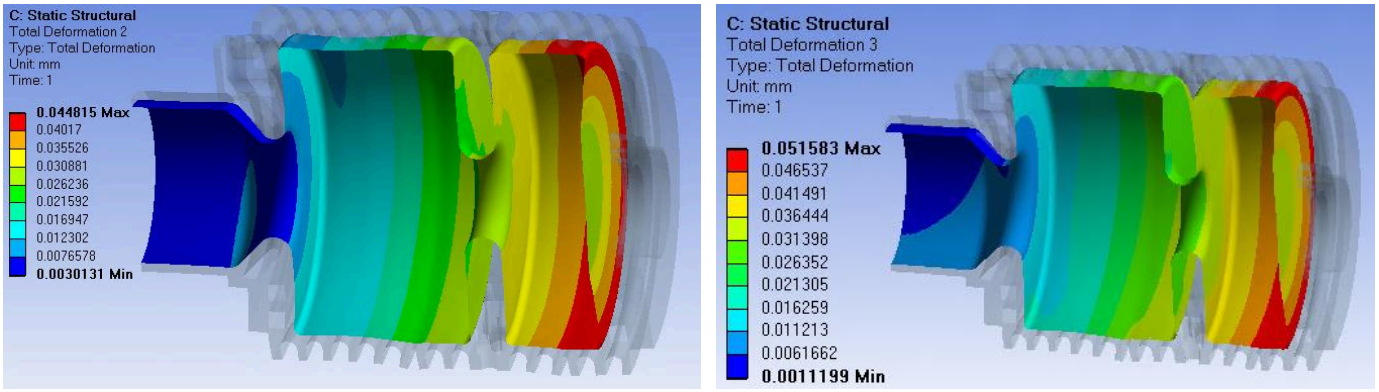

(b) inner surface deformation distribution

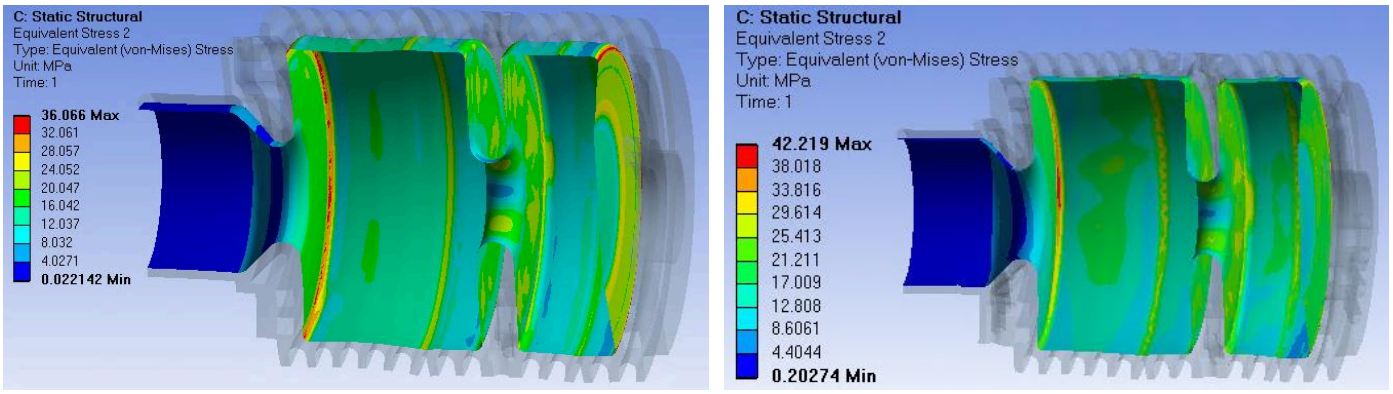

(c) von-Mises stress distribution at the inner surface

Fig. 7. ANSYS simulation results with the empirical heat transfer coefficient (left) and CFX simulated heat transfer coefficient (right) under 40 kW RF heating: (a) temperature distribution, (b) inner surface deformation, (c) inner surface von-Mises stress distribution.

Table 3 lists the main parameters of the RF heating effect on the gun cavity by using different codes and different heat exchange definitions. Simulations using the same empirical heat transfer coefficient show consistent results between CST and ANSYS. The average copper temperature rise obtained with CFX simulated heat transfer coefficient is 20% higher than that obtained with empirical one. As a consequence, the thermal expansion induced cavity deformation and frequency shift are also 20% higher by using CFX simulated heat transfer coefficient than empirical approach. The deviation is attributed to the 10~20% overestimated empirical heat transfer coefficient w.r.t the CFX simulated value, as mentioned in Section 3.1

Table 3. Comparison of RF heating effect on gun frequency by using different codes and different heat exchange definitions.

Parameters	CST with empirical heat transfer coefficient	ANSYS with empirical heat transfer coefficient	ANSYS with CFX simulated heat transfer coefficient
Average power loss [kW]	40	40	40
Average copper temperature rise w.r.t inlet water temperature [°C]	9.7	9.8	11.7
Average inner surface deformation [μm]	24.1	23.2	28.6
Maximum von Mises stress [MPa]	33.1	36.1	42.2
Frequency shift [kHz]	-226.0	-227.3	-274.5
Detuning sensitivity due to RF heating [kHz/kW]	-5.7	-5.7	-6.9

4. High power benchmark measurements

In order to benchmark the simulation results in Section 3.3, high power RF measurements were conducted with the RF gun at PITZ to measure its frequency shift sensitivity to RF heating. In this experiment, the peak power of the RF gun was fixed, and the RF pulse length was varied to change the average RF heating of the gun. The inlet water temperature was used as a frequency tuner to keep the cavity resonant at 1300 MHz at various average power levels with an RF reflection of ~3%, compensating the frequency shift induced by RF heating. Then the cavity frequency change due to the RF heating can be measured with the inlet water temperature change, with a measured sensitivity of 21.8 kHz/°C.

In the measurements, the cathode gradient (57 MV/m) was kept unchanged and the pulse length was scanned from 200 μs to 400 μs with a step of 50 μs. Two methods were used to calculate average power loss at different pulse length. The first one is a straightforward approach by using the inlet and outlet water temperature rise in combination with total water flow. The measurements are shown in Fig. 8. The inlet-outlet temperature rise was increased by only 0.76°C for the 200 μs pulse length case, but a peak to peak temperature fluctuation of ~0.2°C from sensors reading was observed, introducing a significant uncertainty of the RF heating calculation. A detailed error analysis is presented at the end of this section.

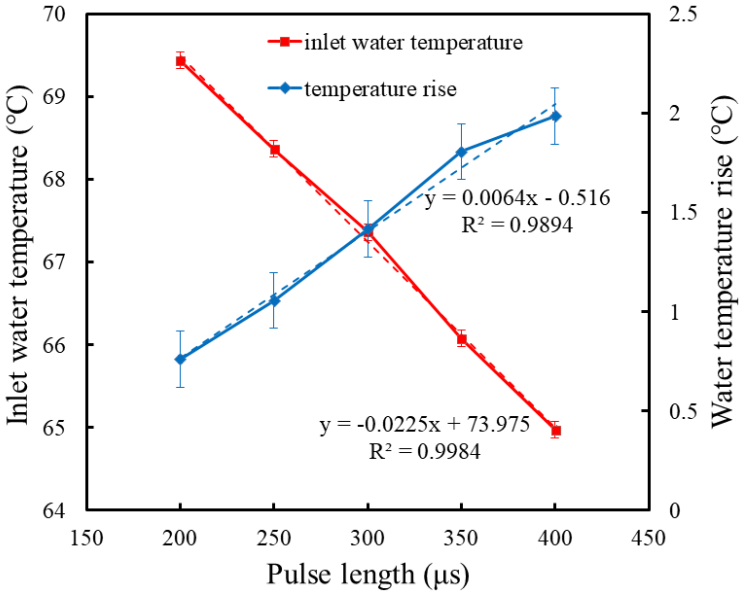

Fig. 8. Inlet water temperature and water temperature rise between inlet and outlet versus RF pulse length.

The second approach is based on the beam energy measurement and the cavity RF properties . The cavity voltage was obtained by the beam energy measurements through a spectrometer dipole magnet in the beamline [8]. The cavity shunt impedance was calculated based on the simulated cavity R/Q and measured unloaded quality factor Q_0. The cavity Q_0 was measured before installing in the beamline. We can also measure Q_0 via the LLRF system when the gun is in operation. Finally, the average cavity power is calculated based on the beam energy, cavity shunt impedance, Q_0 and cavity duty factor, as shown in Eq. (7):

$$P_c = \frac{V_{beam}^2}{\left(\frac{R}{Q}\right)Q_0} DF \tag{7}$$

where V_{beam} is the cavity voltage measured by the maximum beam energy gain, R/Q is simulated from cavity geometry, DF is the RF duty factor of the cavity. The accuracy of the RF heating calculation depends on the beam energy and Q_0 measurements.

The gun Q_0 was measured to be 20472 by a vector network analyzer (VNA) at a room temperature (~20°C). The operation temperature of the current gun is ~70°C resulting in a lower Q_0 because the copper conductivity reduces with rising temperature. With the cavity filling time calculated from the reflected power decay slope (see Fig. 9) and the cavity coupling factor calculated from the smith chart program in the LLRF system, one can obtain the online measurement of Q_0. The simulations and measurements are listed in Table 4. The difference between the LLRF online measurement and the scaled results from offline VNA measurement is only 5%. A Q_0 of 19195 (average of VNA measurement and LLRF measurement) with an error of +/- 480 is used in the following analysis. The measured Q_0 is ~10% lower than the ideal simulation values at 70 °C, which is reasonable in cavity development.

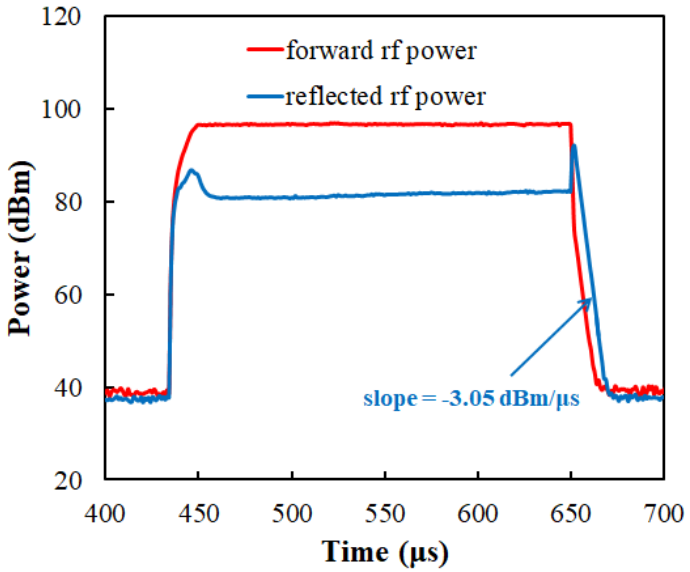

Fig. 9. Forward and reflected RF power waveform extracted from the directional couplers. The decay slope of the reflected power is -3.05 dBm/μs, corresponding to the cavity filling time constant of 2.84 μs.

Table 4. Unloaded quality factor Q_0 simulations and measurements.

	Simulation at 20°C (Cu conductivity = 5.80E7 S/m)	Simulation scaled to 70°C (Cu conductivity = 4.86E7 S/m)	VNA measurement at room temperature ~20°C	VNA measurement scaled to 70°C	LLRF measurement in high power at 70°C
Q_0	23240	21246	20472	18715	19674

Fig. 10(a) shows the average power loss as a function of the RF pulse length by using the previously mentioned two approaches. The error bar of the red dotted curve corresponds to the +/- 0.1°C peak to peak water temperature measurement fluctuation. The error bar of the black line corresponds to the +/- 480 error in Q_0 measurements. The power measurement results by the two approaches are barely within their error bars. Fig. 10(b) shows the cavity frequency shift induced by the RF heating. The cavity frequency sensitivity to RF power is fitted to be -7.11 ± 0.43 kHz/kW based on the power measured by the cavity Q_0 and beam energy, and -5.50 ± 0.78 kHz/kW based on the power measured by the water temperature rise. Due to the large uncertainty caused by the water temperature measurement, the frequency sensitivity of -7.11 ± 0.43 kHz/kW is more reliable. The simulation result of -6.9 kHz/kW based on the CFX simulated heat transfer coefficient in Table 3 is in better agreement with the measurement than simulations with empirical heat transfer coefficient.

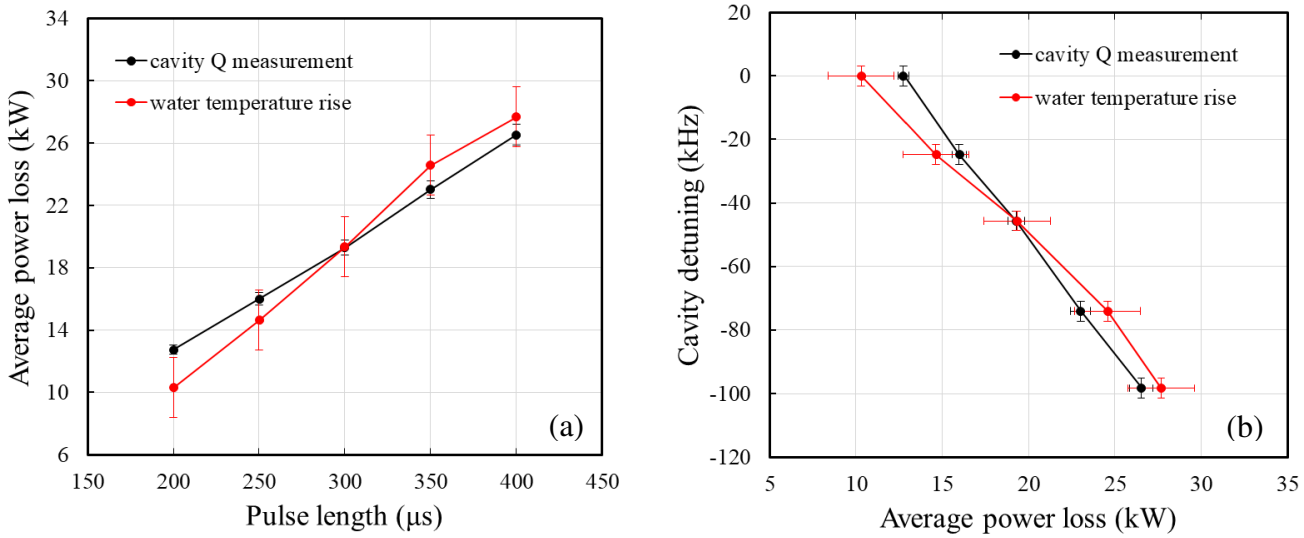

Fig. 10. (a) average power loss vs. pulse length, (b) cavity detuning vs. average power loss.

A few temperature sensors are placed inside the middle iris and one of them is used as a feedback for a water temperature regulation system. The comparison between sensor measurements and ANSYS simulations with empirical and CFX simulated heat transfer coefficients is shown in Fig. 11. The RF pulse length in the measurement was 300 μs and the average power loss was calculated to be 18 kW. Again, the overestimation of heat transfer coefficients based on empirical formulas leads to a lower temperature rise compared to the simulated heat transfer coefficients. The sensor temperature values are shown in Fig. 11 by red numbers. From the sensor calibration test, the bottom sensor in Fig. 11 indicated a worse performance than the other three, therefore it might be damaged by radiation from the gun. One contribution to the discrepancy between the top three sensor measurements and simulations can be the sensor calibration error. In addition, the thermal contacts from the surrounding parts (e.g. load-lock system, doorknob coupler and support bracket) were ignored in the simulation, which leads to an overestimation on simulated temperature. The details of the sensor installation were also ignored in simulation, which might be another reason for the discrepancy. Since the accuracy of the gun frequency measurement is much higher than gun iris temperature measurement, the benchmark of frequency sensitivity is more reliable than temperature.

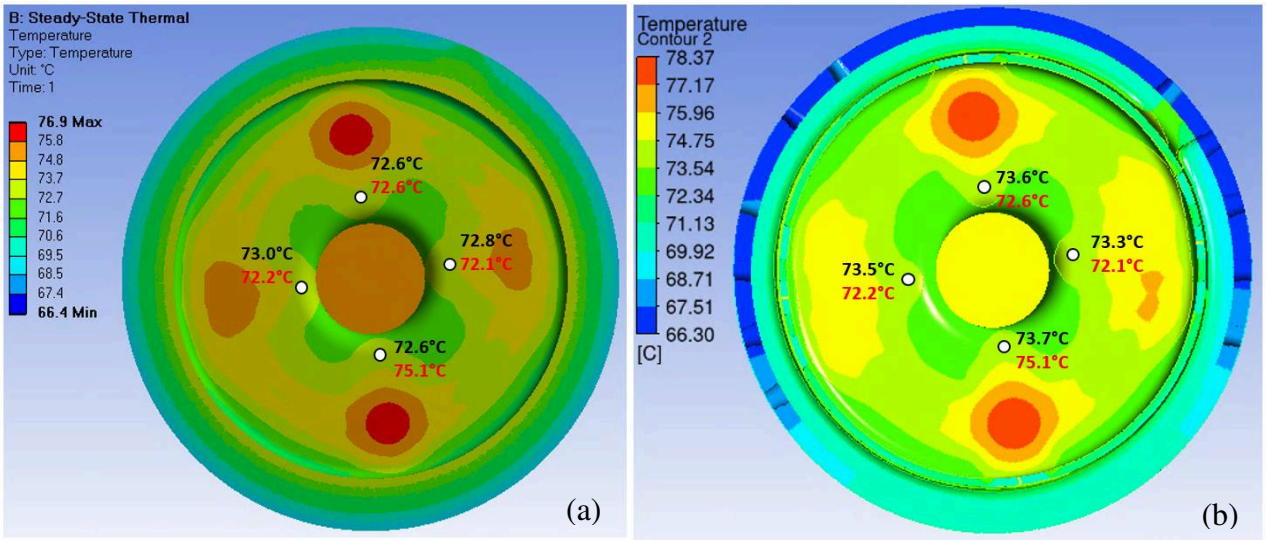

Fig. 11. Iris temperature distribution calculated from ANSYS with (a) empirical heat transfer coefficient and (b) CFX simulated heat transfer coefficient. The simulated temperatures at the sensor position are marked in black. Temperature measurements in experiments are marked in red for comparison.

5. Discussion

The heat transfer coefficient is of paramount importance in multiphysics simulations of RF cavities. If a high power experiment is available, we can evaluate the heat exchange between water and cavity by data fitting with the experiment, which was adopted in Ref. [17]. In the design stage, the precise heat transfer coefficient definition is crucial to obtain reliable predictions. In case of the benchmark simulations of the Gun 4, the heat transfer coefficient calculated from the empirical approximation is overestimated by ~20%. As a consequence, the cavity temperature rise, deformation and frequency shift are underestimated by ~20%. In contrast, the benchmark simulation with the heat transfer coefficient derived from ANSYS CFX simulation is in much better agreement with the experiments. Therefore, the simulated heat transfer coefficient is preferred in the design stage to predict the cavity performance in the high average RF power regime. However, the CFX simulation always takes a long time to reach convergence which is tedious in the cooling channel optimization. The empirical approach is more suitable in the optimization process. Another critical point in the thermal simulation with the empirical approach is the water temperature definition. For the low average power cavity, in which the water temperature rise in the channel can be ignored, the inlet water temperature can be applied on the channel surface in the simulation. For a heavy RF loaded cavity like the Gun 4, the inlet to outlet temperature rise is ~30% of the gun average temperature rise. The mean value of the inlet and outlet temperature should be used, otherwise the average gun temperature will be underestimated.

6. Conclusion

We performed an experimental benchmarking of the integrated multiphysics simulations for the DESY Gun 4, including the electromagnetic, thermal and mechanical simulations. The multiphysics simulations are done with two codes, CST and ANSYS. The heat transfer coefficient calculation in the thermal module proves to be most critical. The multiphysics simulations with empirical values underestimate the RF heating induced temperature rise, deformation, stress and frequency detuning by ~20% for the Gun 4. The simulation results with CFX simulated heat transfer coefficient agree well with measurements. For the cooling analysis of a heavy heat load cavity, the simulated heat transfer coefficient is highly recommended for more accurate results, based on which a more appropriate safety margin can be used in engineering designs.

Acknowledgements

We would like to thank S. Lal, W. Koehler and J.Schultze for valuable discussions. This work was supported by the European XFEL research and development program. The numerical simulation research was supported in part through the European XFEL and DESY funded Maxwell computational resources operated at Deutsches Elektronen-Synchrotron (DESY), Hamburg, Germany.

Reference

[1] W. Decking, et al., A MHz-repetition-rate hard X-ray free-electron laser driven by a superconducting linear accelerator,

Nature Photonics (2020): 1-7.
[2] S. Siegfried and B. Faatz, The free-electron laser FLASH, High Power Laser Science and Engineering 3 (2015).
[3] R. Akre, et al., Commissioning the linac coherent light source injector, Phys. Rev. ST Accel. Beams, 11 (2008), 030703.
[4] T. Schietinger, et al., Commissioning experience and beam physics measurements at the SwissFEL Injector Test Facility, Phys. Rev. Accel. Beams, 19 (2016), 100702.
[5] D. Angal-Kalinin, et al., Design, specifications, and first beam measurements of the compact linear accelerator for research and applications front end, Physical Review Accelerators and Beams, 23 (2020), 044801.
[6] G. Penco, et al., Optimization of a high brightness photoinjector for a seeded FEL facility, Journal of Instrumentation, 8(05), P05015.
[7] F. Sannibale, et al., Advanced photoinjector experiment photogun commissioning results, Physical Review Special Topics-Accelerators and Beams, 15 (2012), 103501.
[8] F. Stephan, et al., Detailed characterization of electron sources yielding first demonstration of European X-ray Free-Electron Laser beam quality, Phys. Rev. ST Accel. Beams, 13 (2010), 020704.
[9] M. Krasilnikov, et al., Experimentally minimized beam emittance from an L-band photoinjector, Phys. Rev. ST Accel. Beams, 15 (2012), 100701.
[10] I. Isaev, et al., Conditioning status of the first XFEL gun at PITZ, 35th Free Electron Laser Conf. (FEL'13), New York, USA, 26-30 August 2013.
[11] V. Paramonov, et al., Design of an L-band normally conducting RF gun cavity for high peak and average RF power, Nuclear Instruments and Methods in Physics Research Section A: Accelerators, Spectrometers, Detectors and Associated Equipment 854 (2017): 113-126.
[12] S. V. Kutsaev, et al., Design and multiphysics analysis of a 176 MHz continuous-wave radio-frequency quadrupole, Physical Review Special Topics-Accelerators and Beams, 17 (2014), 072001.
[13] G. Romanov, et al., CW room temperature re-buncher for the Project X front end, Conf. Proc. C1205201: 3880-3882, 2012. No. FERMILAB-CONF-12-129-TD.
[14] T. Takahashi, et al., Development of a 1.3-GHz buncher cavity for the compact ERL, Proc. 5th International Particle Accelerator Conf.(IPAC 2014), Dresden, Germany, 15-20 June 2014.
[15] R. P. Wells et al., Mechanical design and fabrication of the VHF-gun, the Berkeley normal-conducting continuous-wave high-brightness electron source, Review of Scientific Instruments, 87 (2016), 023302.
[16] G. Shu, et al., Multiphysics Analysis of a CW VHF Gun for European XFEL, 39th Free Electron Laser Conf.(FEL'19), Hamburg, Germany, 26-30 August 2019.
[17] Y. Kondo, et al., High-power test and thermal characteristics of a new radio-frequency quadrupole cavity for the Japan Proton Accelerator Research Complex linac, Physical Review Special Topics-Accelerators and Beams 16 (2013), 040102.
[18] K. Floettmann, et al., RF Gun cavities cooling regime study, DESY report, TESLA-FEL, 2, 2008.
[19] F. Marhauser, Finite element analyses for RF photoinjector gun cavities, DESY report, TESLA-FEL, 2, 2006.
[20] B. L. Militsyn, et al., Design of the high repetition rate photocathode gun for the CLARA project, in Proceedings of LINAC'14, Geneva, Switzerland, 31 August-05 September 2014.
[21] V. Paramonov, A. Skasyrskaya, Pulsed RF heating simulations in normal conducting L-band cavities, DESY, Hamburg, Rep. TESLA-FEL 2007-04, 2007.
[22] D. Pritzkau, RF Pulsed Heating, Ph. D Thesis, SLAC-R-577, 2001.
[23] CST Simulation packages, http://www.cst.com.
[24] ANSYS, http://www.ansys.com.
[25] T.Wangler, RF Linear Accelerators[M]. RF Linear Accelerators, by Thomas Wangler, pp. 397. ISBN 0-471-16814-9. Wiley-VCH, May 1998. 2008.
[26] F. Kreith, The CRC Handbook of Thermal Engineering (CRC Press, Boca Raton, 2000).